

# Plateau de Bure Interferometer Observations of the Disk and Outflow of HH 30<sup>★</sup>

J. Pety<sup>1,2</sup>, F. Gueth<sup>1</sup>, S. Guilloteau<sup>3</sup>, and A. Dutrey<sup>3</sup>

<sup>1</sup> IRAM, 300 rue de la Piscine, 38400 Saint Martin d'Hères, France.  
e-mail: pety@iram.fr, gueth@iram.fr

<sup>2</sup> LERMA, UMR 8112, CNRS, Observatoire de Paris, 61 av. de l'Observatoire, 75014, Paris, France.

<sup>3</sup> L3AB, UMR 5804, Observatoire de Bordeaux, 2 rue de l'Observatoire, 33270 Floirac, France.  
e-mail: Stephane.Guilloteau@obs.u-bordeaux1.fr, Anne.Dutrey@obs.u-bordeaux1.fr

Received 13 June 2006, Accepted 26 July 2006

## ABSTRACT

**Context.** HH 30 is a well-known Pre-Main-Sequence star in Taurus. HST observations have revealed a flared, edge-on disk driving a highly-collimated optical jet, making this object a case study for the disk-jet-outflow paradigm.

**Aims.** We searched for a molecular outflow, and attempted to better constrain the star and disk parameters.

**Methods.** We obtained high angular resolution ( $\sim 1''$ ) observations of the dust continuum at 2.7 and 1.3 mm, and of the  $^{12}\text{CO}$  J=2–1,  $^{13}\text{CO}$  J=2–1 & J=1–0,  $\text{C}^{18}\text{O}$  J=1–0 emissions around HH 30. A standard disk model is used to fit the  $^{13}\text{CO}$  J=2–1  $uv$ -plane visibilities and derive the disk properties, and the stellar mass. An *ad hoc* outflow model is used to reproduce the main properties of the  $^{12}\text{CO}$  J=2–1 emission.

**Results.** The rotation vector of the disk points toward the North-Eastern jet. The disk rotation is Keplerian: Using a distance of 140 pc, we deduce a mass of  $0.45 M_{\odot}$  for the central star. The disk outer radius is 420 AU. A highly asymmetric outflow originates from the inner parts of the disk. Only its North-Eastern lobe was detected: it presents to first order a conical morphology with a  $30^{\circ}$  half opening angle and a constant ( $12 \text{ km s}^{-1}$ ) radial velocity field. Outflow rotation was searched for but not found. The upper limit of the outflow rotation velocity is  $1 \text{ km s}^{-1}$  at 200 AU of the jet axis.

**Conclusions.** HH 30 is a low mass TTauri of spectral type around M1 and age 1 to 4 Myrs, surrounded by a medium size Keplerian disk, of mass around  $4 \cdot 10^{-3} M_{\odot}$ . It beautifully illustrates the jet-disk-outflow interaction, being so far the only star to display a jet and outflow connected to a well defined Keplerian disk, but reveals a surprisingly asymmetric (one-sided) outflow despite a relatively symmetric jet. Furthermore, these observations do not enable to assign the origin of the molecular outflow to entrainment by the optical jet or to a disk wind. In the latter hypothesis, the lack of rotation would imply an origin in the inner 15 AU of the disk.

**Key words.** Individual: HH30 — stars: formation — stars: circumstellar matter — ISM: dust — ISM: molecules radio lines: molecular

## 1. Introduction

During the last decade, the properties of the circumstellar environment of pre-main-sequence (PMS) stars have been extensively studied. Millimeter arrays, such as the IRAM Plateau de Bure interferometer, routinely provide CO line and continuum images of low-mass PMS stars which show that many of them are surrounded by large ( $R_{\text{out}} \sim 200\text{--}800 \text{ AU}$ ) disks in Keplerian rotation (e.g. Koerner et al. 1993; Dutrey et al. 1994; Mannings et al. 1997; Guilloteau & Dutrey 1998; Simon et al. 2000). For several sources, the angular resolution and sensitivity of the observations enable to fit disk models to the data, hence constraining physical parameters of the disk, and even the mass of the central source (Dutrey et al. 2006, and references therein). While mm continuum observations are sensitive to the dust thermal emission of the disk, near-infrared (NIR) or optical observations can be used to trace the stellar light scattered by particles at the disk surface (e.g. Roddier et al. 1996). If the system is edge-on, the disk itself can be seen as a dark lane on the equatorial plane

(e.g. HH 30: Burrows et al. (1996), GM Auriga: Stapelfeldt & The WFPC2 Science Team (1997)).

Most of pre-main-sequence stars also show an ejection of matter. In several sources, optical linear jets are observed through the emission of forbidden atomic lines. Interestingly, Bacciotti et al. (2003) and Coffey et al. (2004) have detected possible rotation signatures in at least four jets (DG Tau, TH 28, RW Aur, LkH $\alpha$  321): They have observed systematic velocity differences between opposite sides of the jet axis. Indeed, rotation of the jet is predicted by magnetocentrifugal models of accretion-ejection (Konigl & Pudritz 2000; Shu et al. 2000), through the coupling of the outflowing gas to the helicoidal structure of the magnetic field. In younger, more embedded sources, large molecular outflows are observed, mainly through the emission of the rotational lines of CO and its isotopologues (Arce et al. 2006, and references therein). Those molecular outflows are usually identified with ambient molecular gas that has been entrained and thus put into motion by the underlying protostellar jet. In any case, it is particularly interesting to check whether a rotation component is present in molecular outflows.

In this context, one of the most interesting objects is the young PMS star HH 30, located in the Taurus molecular cloud

Send offprint requests to: J. Pety, e-mail: pety@iram.fr

<sup>★</sup> PdBI is operated by IRAM, which is supported by INSU/CNRS (France), MPG (Germany), and IGN (Spain).

**Table 1.** Observation parameters.

Phase center $\alpha_{2000} = 04^h31^m37.47^s$ $\delta_{2000} = 18^\circ12'24.2''$								
Molecule & Line	Frequency GHz	Beam arcsec <sup>2</sup>	PA °	$\delta v^a$ km s <sup>-1</sup>	1 $\sigma$ noise levels <sup>a</sup>		Int. Time <sup>b</sup> hours	Obs. Date
HCO <sup>+</sup> J=1-0	89.188	4.28 × 3.33	48	0.4	10	0.11	6	1997–1998
<sup>12</sup> CO J=2-1	230.538	1.78 × 1.16	14	0.4	29	0.32	6	1997–1998
C <sup>18</sup> O J=2-1	109.782	3.49 × 2.82	35	0.3	9	0.09	14	2000–2002
<sup>13</sup> CO J=1-0	110.201	3.48 × 2.81	34	0.3	9	0.09	14	2000–2002
<sup>13</sup> CO J=2-1	220.399	1.80 × 1.56	26	0.3	22	0.20	14	2000–2002

<sup>a</sup> The rms noises are computed from the channel maps featured in Fig. 2 and 3, *i.e.* using natural weighting and the  $\delta v$  channel resolutions of the maps. The original correlator resolution are between 3 and 6 times higher than the one shown here.

<sup>b</sup> This is the total *on-source* observing time of useful data as if all observations were done with 5 antennas.

at a distance of  $\sim 140$  pc. Burrows et al. (1996) obtained spectacular images with the Hubble Space Telescope that revealed a flared edge-on disk of diameter  $\sim 450$  AU, separated in two parts by a dust lane, and a highly-collimated jet emanating out of the central region. Since then, the HH 30 disk and jet have been studied in many details (*e.g.* Bacciotti et al. 1999; Stapelfeldt et al. 1999; Wood et al. 2000; Cotera et al. 2001; Wood et al. 2002; Watson & Stapelfeldt 2004). Stapelfeldt et al. (1999) reported variability and asymmetry in the emission from the circumstellar disk by comparing HST optical observations performed between 1994 and 1998; the photometric variability of the star and its possible effects on the disk was investigated by Wood et al. (2000). This source is a unique candidate to probe the complex interaction between the disk, the jet and the outflow.

However, HH 30 has been poorly investigated at mm wavelengths so far. This is probably due to the confusion arising from the HH 30 parent molecular cloud, which increases the complexity of any detailed observations using the emission of CO isotopologues. The <sup>12</sup>CO emission of the cloud is expected to be optically thick, hence hiding significantly the disk emission. BIMA observations of the <sup>13</sup>CO J=1-0 emission in the environment of HL Tau (Fig. 2 of Welch et al. 2000) shows that HH 30 is located in the south edge of a shell driven by XZ Tau. Still, the remarkable properties of HH 30 makes it a textbook case for the study of the disk/jet system in young PMS stars, and we have therefore decided to use the IRAM Plateau de Bure interferometer to perform high angular resolution ( $\sim 1''$ ) observations of the emission of the circumstellar material surrounding HH 30 in several CO isotopologues lines. In this paper we present the results of this study and the analysis of the thermal dust and molecular line emissions of the disk and the outflow.

## 2. Observations and data reduction

### 2.1. <sup>12</sup>CO, HCO<sup>+</sup> and continuum at 3.4 and 1.3 mm

First PdBI observations dedicated to this project were carried out with 5 antennas in BCD configurations (baseline lengths from 24 to 280 m) during the winter 1997/1998. The observations were performed simultaneously at 89.2 GHz (HCO<sup>+</sup> J=1-0) and 230.5 GHz (<sup>12</sup>CO J=2-1). One correlator band of 10 MHz was centered on the HCO<sup>+</sup> J=1-0 line. Another band of 20 MHz was centered on the <sup>12</sup>CO J=2-1 line. Finally, two bands of 160 MHz were used for the 1.3 mm and 3.4 mm continuum, respectively.

Those observations were part of the survey of protoplanetary disks which is described by Simon et al. (2000). The interferometer was operating in track sharing mode, *i.e.* each 8h-

track was shared between several close-by sources. The *total on-source* observing time dedicated to HH 30 was about 6 hrs. The rms phase noises were between 8 and 25° at 3.4 mm and between 15 and 50° at 1.3 mm. This introduced position errors of  $< 0.1''$ . The seeing, estimated from observations of the calibrators, was  $\sim 0.3''$ . Typical resolutions are 3.6'' at 3.4 mm and 1.4'' at 1.3 mm.

### 2.2. <sup>13</sup>CO, C<sup>18</sup>O and continuum at 2.7 and 1.35 mm

As a follow-up, we carried out observations of <sup>13</sup>CO and C<sup>18</sup>O at PdBI with 5 antennas in CD configuration (baseline lengths from 24 to 176 m) in December 2000, February 2001 and March 2002. The C<sup>18</sup>O J=1-0, <sup>13</sup>CO J=1-0 and <sup>13</sup>CO J=2-1 lines were observed simultaneously using the 3 mm receiver (tuned at 109.9 GHz) and the 1 mm receivers (tuned at 220.4 GHz). Three 20 MHz correlator bands were centered on the C<sup>18</sup>O J=1-0, <sup>13</sup>CO J=1-0 and <sup>13</sup>CO J=2-1 lines. Two bands of 320 MHz were used for the 1.35 mm and 2.7 mm continuum, respectively.

The rms phase noises were between 10 and 25° at 2.7 mm and between 20 and 50° at 1.35 mm. The *total on-source* observing time was about 14 hrs. Typical resolutions are 3'' at 2.7 mm and 1.7'' at 1.35 mm.

### 2.3. Data reduction

All data were reduced using the GILDAS<sup>1</sup> softwares supported at IRAM (Pety 2005). Standard calibration methods using close calibrators were applied to all the PdBI data. Images were produced using natural weighting of the visibilities for the line maps and robust weighting for the continuum maps.

The 1.30 mm and 1.35 mm continuum observations were merged (after flux correction using a spectral index of 2.22, see Section 3.3) to produce a map of higher signal-to-noise ratio in Fig. 1. The channel maps presented in Figs. 2 and 3 include the continuum emission because it is *in this case* weak compared to the line emission. It has nonetheless been subtracted before fitting the disk (*cf.* section 4.1).

## 3. Results

All observed lines were detected although with very different strengths. <sup>12</sup>CO J=2-1, <sup>13</sup>CO J=1-0 and <sup>13</sup>CO J=2-1 emissions

<sup>1</sup> See <http://www.iram.fr/IRAMFR/GILDAS> for more information about the GILDAS softwares.

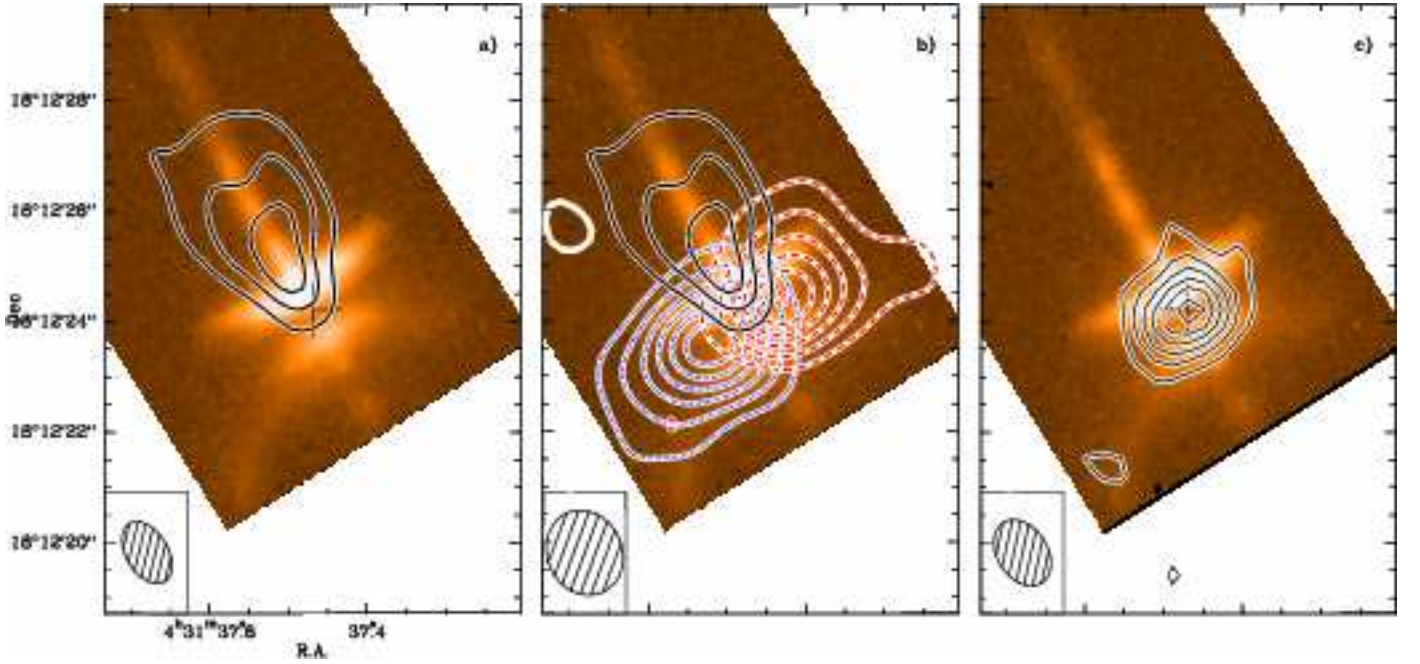


**Fig. 1.** Left panel: Contours of the  $^{12}\text{CO}$  J=2–1 emission of HH 30 are plotted over a composite HST image (670 and 787.7 nm, see Burrows et al. 1996). Emission is only integrated at extreme velocities ( $\leq 4 \text{ km s}^{-1}$  and  $\geq 11 \text{ km s}^{-1}$ ) to avoid contamination by the disk emission. Contours are at the 3-sigma level (48 mJy/Beam) and the spatial resolution is  $1.23 \times 0.75''$  PA  $31^\circ$  (compared to a pixel size of  $0.1''$  for the HST image). Medium panel : Superimposition of 3-sigma level contours 1) of the outflow emission as traced by the  $^{12}\text{CO}$ (2–1) emission integrated at extreme velocities (cf. left panel) and 2) of the blue-shifted from  $4.6$  to  $7.2 \text{ km s}^{-1}$  (blue dotted line, 29 mJy/Beam) and red-shifted from  $7.2$  to  $9.8 \text{ km s}^{-1}$  (red dashed line, 29 mJy/Beam) emission of the disk as traced by the  $^{13}\text{CO}$ (2–1) line. The spatial resolution of the  $^{13}\text{CO}$  map is  $1.57 \times 1.35''$  PA  $25^\circ$ . Right panel: Superimposition of the 3-sigma level (1.4 mJy/Beam) of the merged 1.30 mm and 1.35 mm continuum emission over the same composite HST image. The spatial resolution is  $1.29 \times 0.91''$  PA  $33^\circ$ .

**Table 2.** Continuum fluxes and sizes as a function of the frequency.

Frequency (GHz)	Wavelengths (mm)	Flux (mJy)	Gaussian FWHM ( $''$ )	Gaussian PA ( $^\circ$ )	Beam FWHM ( $''$ )	Beam PA ( $^\circ$ )
89.2	3.40	$2.5 \pm 0.5$	$< 2$ ( <i>i.e.</i> unresolved)	—	$4.28 \times 3.33$	47
110.0	2.65	$3.8 \pm 0.2$	$< 2$ ( <i>i.e.</i> unresolved)	—	$2.86 \times 2.25$	36
220.4	1.35	$18.1 \pm 0.7$	$1.28 \pm 0.10 \times 0.53 \pm 0.12$	$-51 \pm 6$	$1.82 \times 1.16$	16
230.5	1.30	$23.0 \pm 1.4$	$1.10 \pm 0.20 \times 0.62 \pm 0.12$	$-64 \pm 13$	$1.42 \times 1.22$	30
220.4+230.5	1.35+1.30	$17.3 \pm 0.6$	$1.26 \pm 0.11 \times 0.58 \pm 0.09$	$-50 \pm 5$	$1.29 \times 0.90$	33

are strong while only weak  $\text{C}^{18}\text{O}$  J=1–0 and  $\text{HCO}^+$  J=1–0 emissions are observed. Continuum emission at 3.4 mm, 2.7 mm, 1.35 mm and 1.30 mm is detected, the source being resolved only at 1.30 mm. Fig. 1 summarizes our molecular and continuum observations of HH 30 superimposed over the well-known HST image (Burrows et al. 1996). This figure clearly suggests that 1) the outflow is detected only through the  $^{12}\text{CO}$  emission, 2) the  $^{13}\text{CO}$  J=2–1 line mainly traces the rotating disk (the velocity gradient along the major axis of the optical disk is a direct signature of rotation), and 3) the mm continuum emission, centered on the optical dark lane, is thermal and originates from the disk. Fig. 2 and 3 present the channel maps of the four observed CO lines. Those channel maps are centered around the HH 30 systemic velocity of the disk:  $7.25 \text{ km s}^{-1}$  (cf. Section 4). Only channels where signal is detected are shown, *i.e.* from  $-0.2$  to  $13.8 \text{ km s}^{-1}$  for  $^{12}\text{CO}$  J=2–1 and from  $4.9$  to  $10.3 \text{ km s}^{-1}$  for the other CO isotopologues. As a reference, the optical dark line and jet directions as seen on the HST image are sketched on those figures with orthogonal lines.

### 3.1. The molecular cloud

$^{13}\text{CO}$  J=1–0 channel maps (Fig. 2.b) show emission centered on the optical disk on top of large structures, unrelated to the outflow and/or the disk. Those large structures are clearly seen on the  $^{13}\text{CO}$  J=1–0 emission in the same velocity interval (*i.e.* 6 to  $8.4 \text{ km s}^{-1}$ ), both in the high spatial resolution PdBI data (Fig. 2.b) and in medium spatial resolution but wide field-of-view BIMA data (Fig. 2 of Welch et al. 2000). However, they are not detected on the  $^{13}\text{CO}$  J=2–1 channel maps (Fig. 2.a). We thus identify those large structures with the surrounding molecular cloud. As the disk is expected to be hotter than the molecular cloud, the  $^{13}\text{CO}$  J=2–1 line is mainly originating from the disk while the  $^{13}\text{CO}$  J=1–0 emission shows both contributions. Moreover, the molecular cloud  $^{12}\text{CO}$  J=2–1 emission is expected to be optically thick, hence hiding any emission from the disk/outflow system. Indeed,  $^{12}\text{CO}$  J=2–1 channels from 6.2 to  $7 \text{ km s}^{-1}$  are devoid of signal in the disk/jet directions on Fig. 3. The interferometer has probably filtered out this emission be-

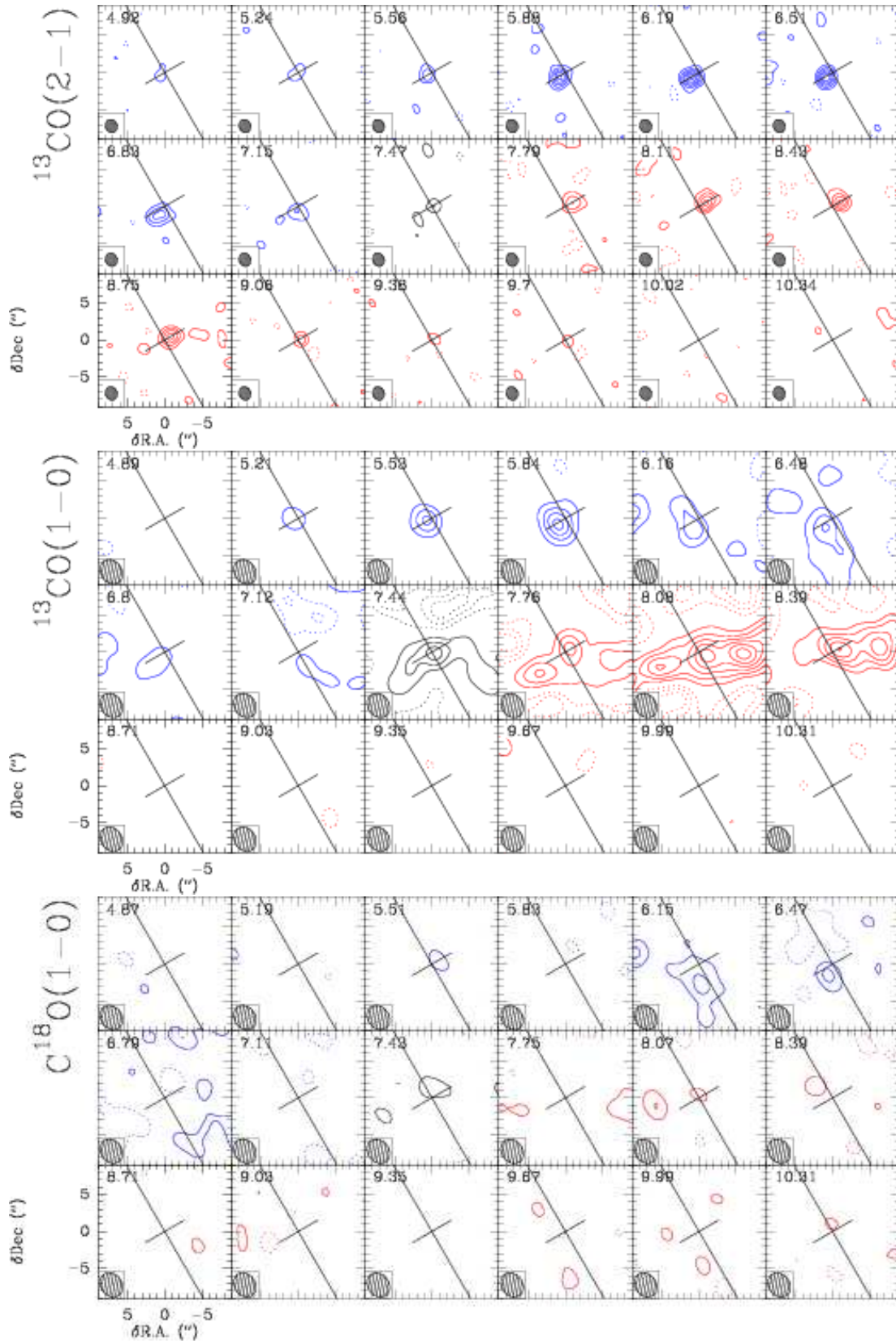


**Fig. 2.** Line emission of the CO isotopologues in HH 30. From top to bottom:  $^{13}\text{CO}$  J=2–1,  $^{13}\text{CO}$  J=1–0, and  $\text{C}^{18}\text{O}$  J=1–0 emissions. The channel maps are centered near  $7.25 \text{ km s}^{-1}$ , the HH 30 systemic velocity. Blue and red contours respectively indicates the blue and red–shifted channels. Channel width is  $0.32 \text{ km s}^{-1}$ . Plain and dotted lines respectively show positive and negative contours. Contour spacing corresponds to  $3 \sigma$  for  $^{13}\text{CO}$  J=1–0 and J=2–1 and  $2 \sigma$  for  $\text{C}^{18}\text{O}$  J=1–0. Noise levels and spatial resolutions may be found in Table 1. The cross indicates the position and orientation 1) of the continuum emission at 1.3 mm and, 2) of the optical jet.

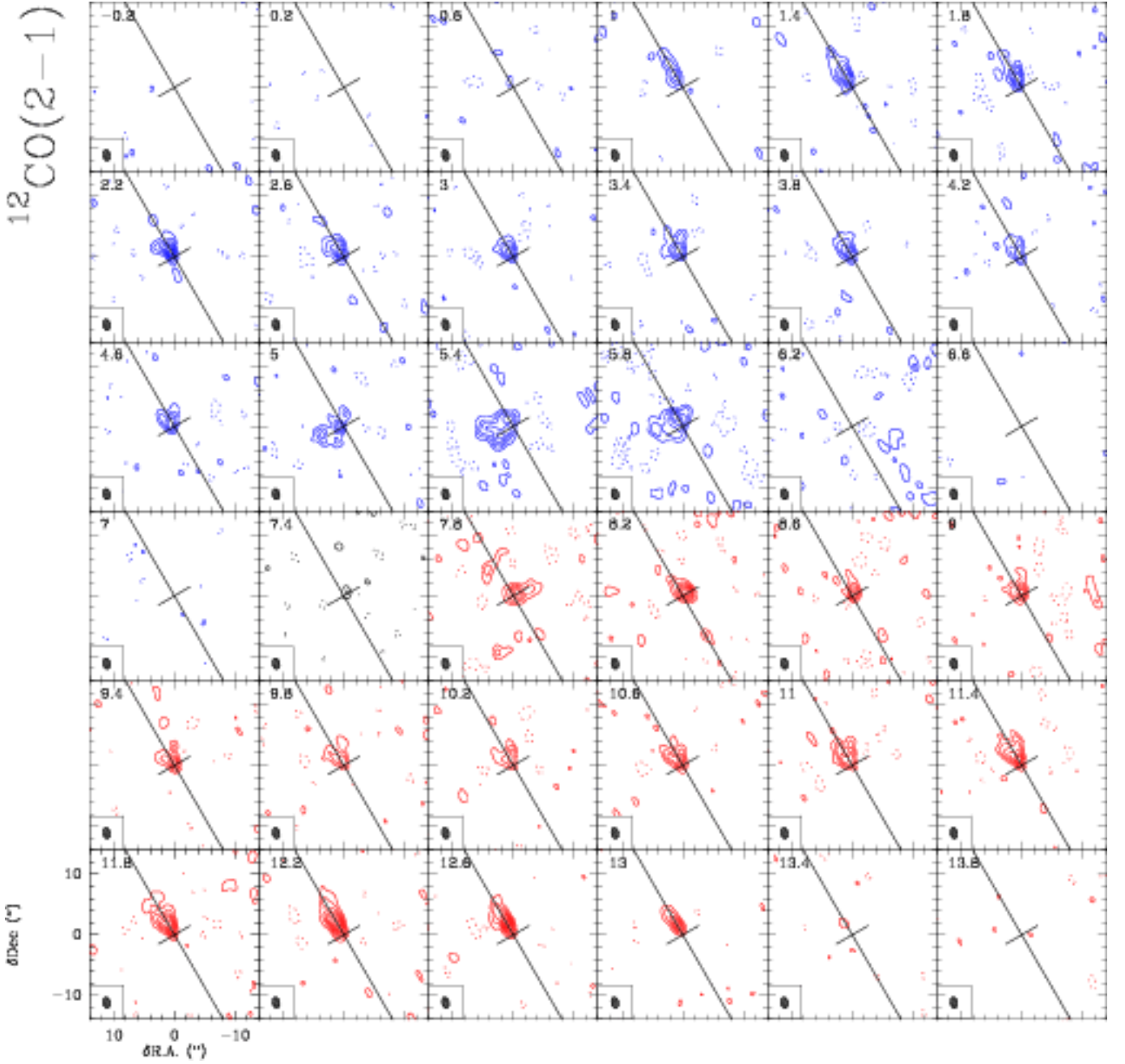


**Fig. 3.** Same as Fig. 2 for the emission of the  $^{12}\text{CO } J=2-1$  line. Spectral resolution is  $0.4 \text{ km s}^{-1}$  and contour spacing correspond to  $3 \sigma$  (cf. Table 1 for more details).

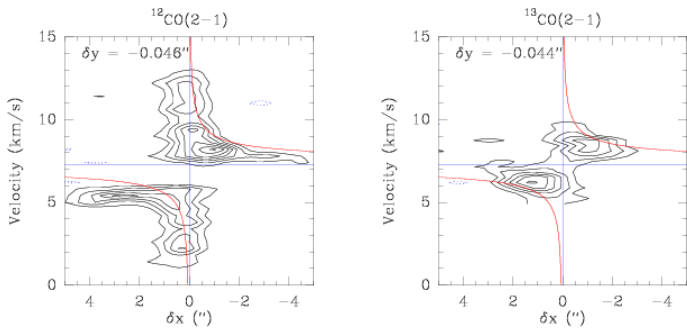
cause the size scale of the optically thick molecular cloud emission is larger than typically half the interferometer primary beam (the well-known short-spacings problem). Finally, the emission of  $\text{C}^{18}\text{O } J=1-0$  (the most optically thin line of this study) is very weak and peaks from  $6.2$  to  $6.8 \text{ km s}^{-1}$  (Fig. 2.c).

### 3.2. The molecular disk

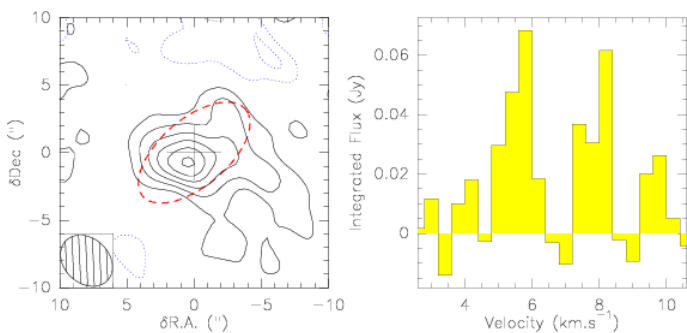
Contrary to  $^{13}\text{CO } J=1-0$  line, the  $^{13}\text{CO } J=2-1$  emission shown in Fig. 2 is clearly dominated by the circumstellar disk. The disk is seen in the  $^{13}\text{CO } J=2-1$  emission from  $\sim 5$  to  $10 \text{ km s}^{-1}$ . The disk is also detected in the same velocity range in the  $^{12}\text{CO } J=2-1$  channel maps (cf. Fig. 3).

Fig. 4.a shows a Position-Velocity plot along the disk axis for  $^{12}\text{CO } J=2-1$  and  $^{13}\text{CO } J=2-1$ . We overplotted 1) the direction of

star and the systemic velocity as two orthogonal blue lines and 2) the curves of the theoretical Keplerian velocity for a  $0.45 M_{\odot}$  star. Note that this is just an illustration: The stellar mass value and uncertainty are determined through the detailed disk analysis described in section 4.2. A clear signature of the Keplerian rotation of the disk is visible. However, some confusion exists from the parent cloud. For  $^{12}\text{CO } J=2-1$ , this confusion is so important that the disk emission stays undetected due to the molecular cloud between  $6.2$  and  $7 \text{ km s}^{-1}$ . For  $^{13}\text{CO } J=2-1$ , the confusion in the disk direction is important only for the  $6.83$ ,  $6.51$  and  $6.19 \text{ km s}^{-1}$  channels and minor elsewhere. The detailed modelling of the HH 30 circumstellar disk described in section 4.2 is thus mainly based on the  $^{13}\text{CO } J=2-1$  data in the velocity range devoid of confusion by the parent cloud.



**Fig. 4.** Position–velocity diagrams along the disk axis of the  $^{12}\text{CO}$  J=2–1 (left panel, contour spacings set to 90 mJy/Beam or  $\sim 3\sigma$ ) and  $^{13}\text{CO}$  J=2–1 (right panel, contour spacings set to 60 mJy/Beam or  $\sim 3\sigma$ ) emissions. The blue horizontal and vertical lines respectively indicate the systemic velocity and the center of the disk as seen in the continuum. The red curves show the theoretical Keplerian velocity for a  $0.45 M_{\odot}$  star.



**Fig. 5. Left:** Integrated emission of the  $\text{HCO}^+$  J=1–0 line in the 5 to 8  $\text{km s}^{-1}$  velocity interval. Contour spacing corresponds to  $1\sigma$  ( $15 \text{ mJy/beam km s}^{-1}$ ). The cross indicates the position of the continuum emission at 1.3 mm. **Right:**  $\text{HCO}^+$  J=1–0 spectrum of the flux integrated over the ellipse shown as a red dash contour on the left panel (size:  $10'' \times 5''$ , with a major axis at PA:  $-50^\circ$ ).

With a critical density of  $n_c \approx 4 \cdot 10^4 \text{ cm}^{-3}$ , the  $\text{HCO}^+$  J=1–0 transition is expected to be thermalized in protoplanetary disks. This transition is also easily observed in molecular clouds with a sub-thermal excitation, and often detectable in molecular outflows. However, the  $\text{HCO}^+$  J=1–0 emission in HH 30 only comes from the disk as illustrated by Fig. 5.

### 3.3. The dust disk

We obtained continuum maps at four different wavelengths: 3.4, 2.7, 1.35, and 1.3 mm. All of them show emission coincident with the HH 30 protostar position. This strongly suggests we are observing thermal emission from the dusty disk. Only the merged 1.35 mm and 1.30 mm continuum map is shown in Fig. 1. As a first analysis, we fitted in the  $uv$  plane a bi-dimensional Gaussian function in each data set. Results are displayed in table 2. The continuum fluxes agree with previous measurements made at OVRO (Stapelfeldt & Padgett 1999). A fit of a power law,  $S_\nu = S_{100}(\nu/100\text{GHz})^\alpha$ , through the measured fluxes yields  $\alpha = 2.22 \pm 0.08$  and  $S_{100} = 3.19 \pm 0.18 \text{ mJy}$ . Low frequency continuum emission is unresolved while a Gaussian fit through the 1.35 mm and 1.30 mm merged data set gives a size of  $1.26 \pm 0.11 \times 0.58 \pm 0.09''$  with a major axis at PA  $-50 \pm 5^\circ$  (i.e. a disk axis at PA  $40 \pm 5^\circ$ ). This orientation is consistent with the orientation of the dark lane in the optical images (disk axis

at PA  $32.2 \pm 1.0^\circ$ , Burrows et al. 1996). Assuming a distance of 140 pc, the fitted linear continuum FWHM is  $\sim 175 \times 80 \text{ AU}$ .

### 3.4. The molecular outflow

The outflow is only detected in the  $^{12}\text{CO}$  J=2–1 emission. However, as said before, there is confusion with the disk and parent cloud emission at velocities close to the HH 30 systemic velocity. Only the channels at extreme velocities ( $\leq 4 \text{ km s}^{-1}$  and  $\geq 11 \text{ km s}^{-1}$ ) can be attributed to the outflow without ambiguities. The integrated image from the outflow and the disk are presented in Fig. 6, showing that the outflow contributes about twice as much to the total flux as the detected disk and parent cloud.

Fig. 3 clearly shows that the CO outflow is essentially one-sided. While the North-East lobe is prominent, there is no emission from South-West, except at low level (3 to 6 sigma) in the velocity range 7.8 to 8.6  $\text{km s}^{-1}$ . In this northern lobe, the  $^{12}\text{CO}$  emission delineates a conical structure, whose apex coincides (within the resolution of these observations) with the star location. The semi-opening angle is  $\sim 30^\circ$ . The highly-collimated jet seen by the HST is located precisely on the axis of this conical  $^{12}\text{CO}$  outflow, in agreement with the usual disk/jet formation paradigm.

As expected from the edge-on geometry of the disk, the outflow lies almost perfectly in the plane of sky. This is indicated by the outflowing gas being observed at both blue and red-shifted velocities in the same (northern) lobe, as well as by the quite low maximal velocities (only  $\sim 6 \text{ km s}^{-1}$ ). Indeed the extreme velocities, 1 and 13.2  $\text{km s}^{-1}$ , are almost exactly symmetric from the systemic velocity determined from  $^{13}\text{CO}$  (7.25  $\text{km s}^{-1}$ ). Assuming the  $^{12}\text{CO}$  emission arises from outflowing gas along the cone wall, with a constant velocity expansion, we can derive an outflow velocity of  $\approx 12 \pm 2 \text{ km s}^{-1}$  and an inclination of  $\approx 0 \pm 2^\circ$ .

Although the molecular outflow is definitely observed as a conical structure emanating from the *inner* part of the disk, CO “clumps” also exist in projection along the jet axis, e.g.  $7''$  NW off the source as illustrated in Fig. 7.

## 4. Disk Model

### 4.1. Analysis method

A standard disk model (Pringle 1981) was used to quantify the properties of the HH 30 circumstellar disk. This model assumes an axi-symmetrical geometry, local thermodynamic equilibrium and the absence of a vertical gradient of temperature. Turbulence is phenomenologically introduced by adding a turbulent width  $\Delta v$  to the thermal width. Radial evolutions of temperature, surface density and velocity are assumed to be power law normalized at 100 AU:  $T = T_{100} (r/100 \text{ AU})^{-q}$ ,  $\Sigma = \Sigma_{100} (r/100 \text{ AU})^{-p}$  and  $V = V_{100} (r/100 \text{ AU})^{-v}$ . A value of 0.5 for the velocity scaling exponent  $v$  implies that the disk rotation is Keplerian. We further assume that the density profile follows a Gaussian distribution of the height  $z$  above the disk plane with the scale height  $H(r)$  being a power law of  $r$

$$n(r, z) = n(r) \exp \left\{ - \left( \frac{z}{H(r)} \right)^2 \right\} \text{ and } n(r) = \frac{\Sigma(r)}{\sqrt{\pi} \cdot H(r)}$$

$$H = H_{100} (r/100 \text{ AU})^h \text{ and } n = n_{100} (r/100 \text{ AU})^{-s}$$

which implies  $s = p + h$  (hydrostatic equilibrium would further imply  $h = 1 + v - q/2$ , see Dartois et al. 2003).

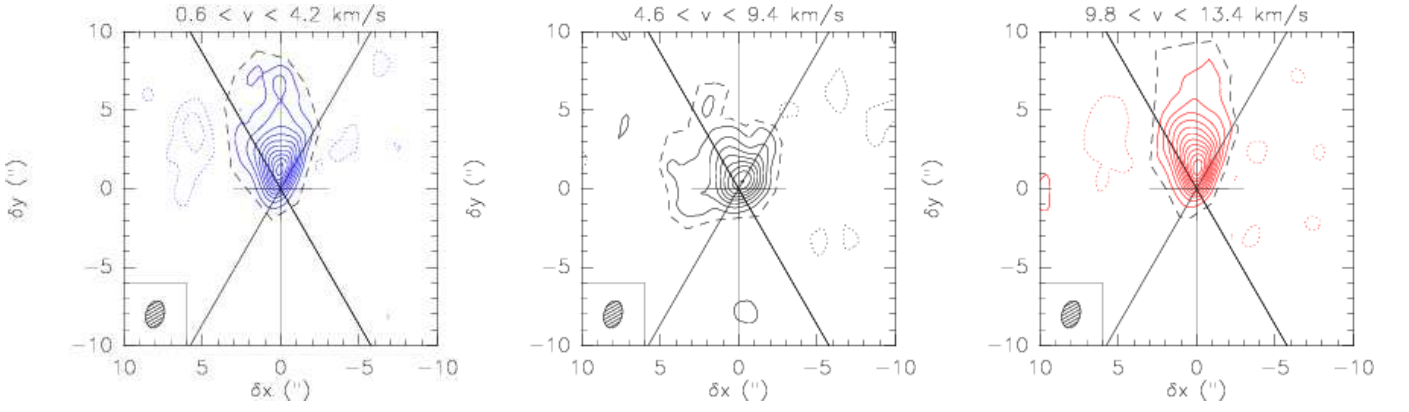


**Fig. 6.** Integrated emissions of the  $^{12}\text{CO}$  J=2–1 line in three contiguous velocity intervals: 1) blue-shifted velocities where only the outflow emits (left panel), 2) near-systemic velocities where confusion arises between the outflow, the disk and the cloud (medium panel), 3) red-shifted velocities where only the outflow emits (right panel). Maps have been rotated by  $30^\circ$  clockwise around the disk center to bring the optical jet direction in the vertical direction as this eases the extraction of position–velocity diagrams. This defines a new coordinate system, named  $x, y$  hereafter. In addition to the horizontal–vertical cross featuring the dark line and the optical jet, a second cross is sketching a cone of  $30^\circ$  half-opening angle. The contour spacing corresponds to  $3\sigma$  (*i.e.* from left to right: 0.16, 0.18 and 0.16 Jy/Beam  $\text{km s}^{-1}$ ). Fluxes estimated inside polygons following the  $2\sigma$  contour (dashed lines) are from left to right: 6.8, 7.0 and 8.3  $\text{Jy km s}^{-1}$ .

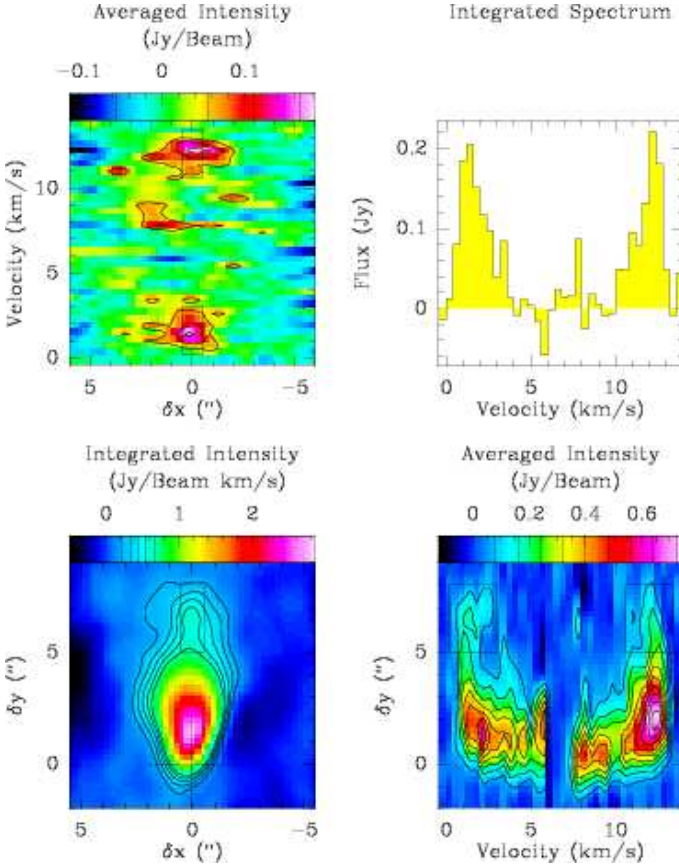


**Fig. 7.** Spatial and kinematical properties of the  $^{12}\text{CO}$  J=2–1 “clump” observed along the jet axis: (a) Top left:  $xv$  position–velocity diagram averaged on  $5'' < \delta y < 8''$ . (b) bottom left: Integrated intensity in the  $[0,3]$  and  $[10.5,13.5]$   $\text{km s}^{-1}$  velocity ranges. (c) Bottom right:  $vy$  position–velocity diagram averaged on  $-0.5'' < \delta x < 0.5''$ . (d) Top right: Spectrum integrated in the  $-0.5'' < \delta x < 0.5'' \times 5'' < \delta y < 8''$  rectangle.

The model parameters are:  $D$  the distance from Earth,  $V_{\text{LSR}}$  the systemic velocity,  $PA$  the plane–of–sky orientation,  $R_{\text{out}}$  the

disk outer radius,  $\Delta v$  the turbulent line width, and the parameters of the power laws ( $\{V_{100}, v\}$ ,  $\{T_{100}, q\}$ ,  $\{H_{100}, h\}$ ) plus a pair  $\{\Sigma_{100}, p\}$  for each molecule transition and for the dust). Since the whole model is described by a limited number of parameters, it is possible to perform a  $\chi^2$  minimization in order to derive the best-fitted values of each parameter. The fitting is performed in the  $uv$  plane to avoid any error introduced by the imaging and deconvolution stages. The  $\chi^2$  is thus defined from the difference between the observed and predicted visibilities:

$$\chi^2 = \sum_{u,v,V} \left| \frac{\text{model}(u, v, V) - \text{observed}(u, v, V)}{\sigma_{(u,v)}} \right|^2$$

where  $\sigma_{(u,v)}$  is the noise associated to each visibility (see Guilloteau & Dutrey 1998). The minimization were done after subtraction of the continuum visibilities from the line  $uv$  table (for details, see Pietu et al. 2006).

The analysis results are summed up in Tables 3 and 4. The comparison between our best model and the observations is shown in Fig. 8 for the  $^{13}\text{CO}$  J=2–1 line.

## 4.2. $^{13}\text{CO}$ lines

### 4.2.1. Fit difficulties

The near edge-on geometry of HH 30 makes this source a special case. First, the model must properly sample the disk thickness to adequately model the line emission. Second, the number of independent data points is actually small since the emission is unresolved perpendicular to the disk plane. This implies a significant degeneracy between parameters  $T_{100}$ ,  $q$ ,  $\Sigma$ ,  $p$ ,  $\Delta v$  and the scale height  $H(r)$ . In fact, the  $^{13}\text{CO}$  J=2–1 line intensity depends weakly on the temperature in the expected temperature range for HH 30, *i.e.* around 20 K for the linear scales sampled (Dartois et al. 2003). At any (non zero) projected velocity  $v_{\text{obs}}$ , the line flux will mostly come from a radius  $r = 100(V_{100}/v_{\text{obs}})^2$ , and the total emitted flux will be essentially proportional to  $\Sigma(r)H(r)\delta V$ , where  $\delta V$  is the local intrinsic line width.

A further difficulty is the existence of contamination by the molecular cloud, and perhaps also by the outflow. We avoided

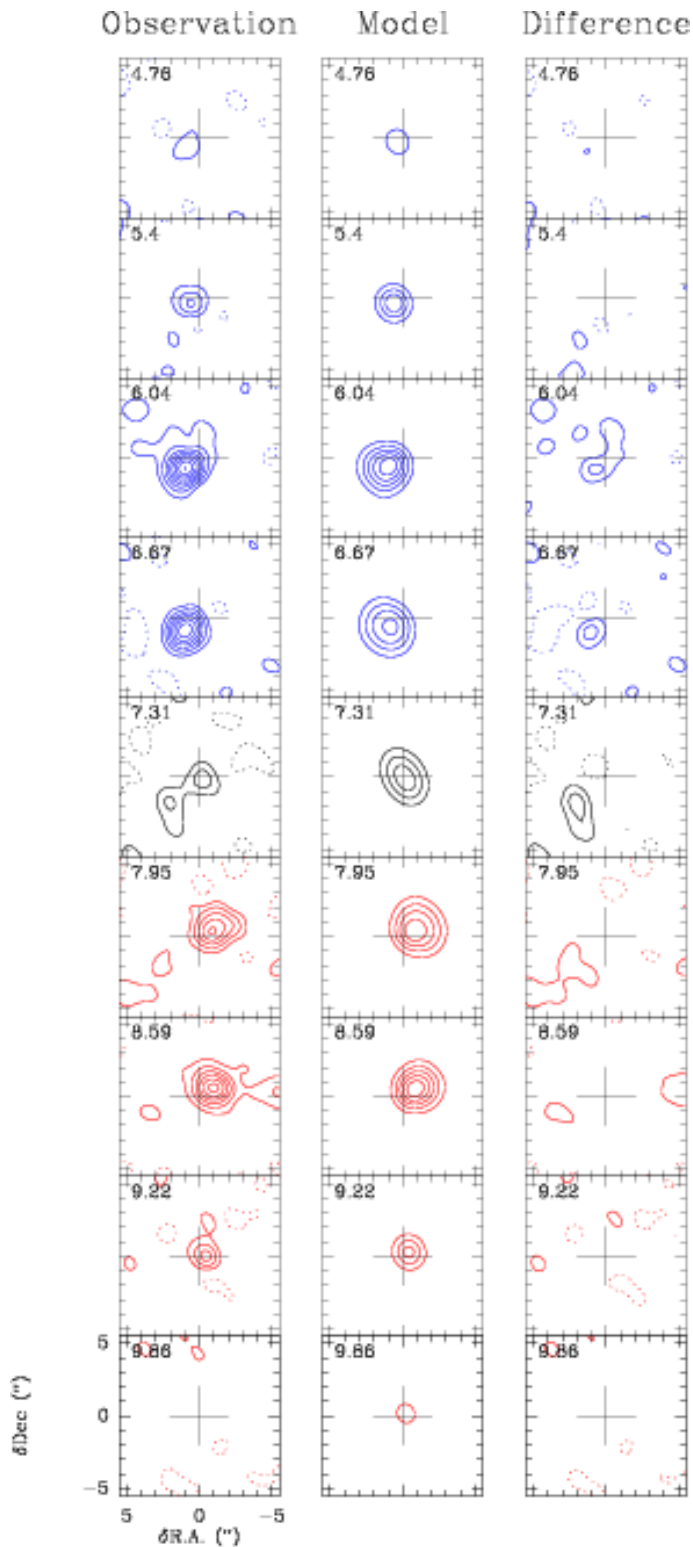


**Fig. 8.** Channel maps of the  $^{13}\text{CO}$  J=2–1 emission. Observations, best model and difference (= observation–model) are plotted from left to right. The coordinate system is native (*i.e.* equatorial). The spatial resolution is  $1.8 \times 1.6''$  at PA of  $26^\circ$ . All contours are equally spaced by a value of 45 mJy/Beam ( $2.5 \sigma$  at the spectral resolution of  $0.64 \text{ km s}^{-1}$ ). Blue and red contours respectively indicate the blue and red–shifted channels while the black contours indicate the systemic velocity channel at  $7.25 \text{ km s}^{-1}$ . Plain and dotted lines respectively show positive and negative contours. The cross indicates the disk center as measured in the 1.3 mm continuum emission. A geometrical asymmetry ( $5\sigma$ –contours in the difference maps) is detected in the blue–shifted part of the disk, close to the systemic velocity.

contamination by the molecular cloud by ignoring the velocity range from  $6.2$  to  $6.8 \text{ km s}^{-1}$  in the determination of the  $\chi^2$ . Any contamination by the outflow would separate from the disk only spatially, not in the velocity space. As the fit is done in the  $uv$  space, contamination by the outflow is unavoidable. Although the outflow contribution is most likely small, because emission at large velocities from the outflow region is not detected in the  $^{13}\text{CO}$  J=2–1 channel maps (see Fig. 8), it may slightly bias the inclination towards lower values.

#### 4.2.2. Fit steps and results

We have performed  $\chi^2$  global minimizations using the following set of parameters: PA,  $i$ ,  $R_{\text{out}}$  to constrain the geometry, and  $V_{\text{lsr}}$ ,  $V_{100}$ ,  $\nu$ , to constrain the velocity power law, using fixed values for the other parameters (see Table 3). The systemic velocity value of  $7.25 \text{ km s}^{-1}$  quoted before comes from this step. We verified that the rotation is Keplerian on the pair of parameters ( $V_{100}$ ,  $\nu$ ). This again suggests that any remaining confusion due to the outflow or cloud is small. We found HH 30 to be essentially edge on, with a best fit inclination  $\approx 81^\circ$ . We nevertheless fixed the inclination to  $84^\circ$  in all other fits to avoid the possible inclination bias due to the outflow contamination (see above). We verified that all other parameters are essentially independent on this small variation of the inclination.

The degeneracy between the remaining parameters cannot be fully removed with the available data. We thus assumed the height law parameters to be  $H_{100} = 22 \text{ AU}$ , and  $h = 1.25$ . We then fitted the J=1–0 and J=2–1 lines of  $^{13}\text{CO}$  simultaneously. We find for the temperature law:  $T = 12 \pm 1 \text{ K}$ ,  $q = 0.55 \pm 0.07$ . The associated  $^{13}\text{CO}$  surface density at 100 AU is about  $9 \cdot 10^{16} \text{ cm}^{-2}$  (with a factor two uncertainty), but the surface density power law index  $p$  is less well constrained:  $p \approx 1.5 \pm 1$ .

Temperature and density power laws are less certain because 1) the simultaneous fit is only valid in the absence of strong vertical temperature gradient and 2) the constraint uses only a few channels from the J=1–0 line of  $^{13}\text{CO}$  where the contamination by the parent cloud is thought negligible. We nevertheless stress that our assumptions have essentially no influence on the main disk parameters,  $V_{100}$ ,  $i$ , and  $R_{\text{out}}$ , which are well constrained by the current data.

#### 4.3. $\text{HCO}^+$ J=1–0 line

$\text{HCO}^+$  emission is detected from the disk, but with a relatively low signal–to–noise ratio. There is *no* evidence of  $\text{HCO}^+$  emission either from the cloud or from the outflow. Accordingly, the  $\text{HCO}^+$  data were analyzed in a very similar way to the  $^{13}\text{CO}$  data, but all channels were included in the analysis. The results (*e.g.* outer radius) agree within one sigma with those obtained from  $^{13}\text{CO}$ , but the error bars are large. In practice, only the  $\text{HCO}^+$  column density is constrained from these observations. Using  $p = 1.5$  and  $R_{\text{out}} = 400 \text{ AU}$ , we find  $\Sigma[\text{HCO}^+] = 7.2 \pm 1.5 \cdot 10^{12} \text{ cm}^{-2}$  at 100 AU.

#### 4.4. Continuum Emission

We have high resolution continuum observations at four different frequencies. As the disk dust thermal emission is at least marginally resolved and partially optically thin, we may obtain an *independent estimate of the outer radius and the surface density*. Matching the surface density found in this process with the

one derived from the  $^{13}\text{CO}$  data enables to derive the abundance of  $^{13}\text{CO}$ .

We used the disk model derived from the  $^{13}\text{CO}$  data and the four continuum measurements to constrain the dust emissivity index,  $\beta$ , and the surface density  $\Sigma_{100}$  assuming the emissivity law is given by  $\kappa(\nu) = 0.1(\nu/10^{12}\text{Hz})^\beta \text{ cm}^2\text{g}^{-1}$ . We made a global  $\chi^2$  fit using the following four parameters:  $R_{\text{out}}$ ,  $\beta$ ,  $\Sigma_{100}$  and  $p$ .

**Table 3.** Comparison of mm and optical/NIR properties. The upper part of the table shows parameters whose value is robustly deduced from the millimeter data (geometry, velocity law and stellar mass) while the bottom part displays parameters less well constrained due to the limited vertical resolution of this edge-on disk. Most parameters are deduced from the analysis of the  $^{13}\text{CO}$  emission, except for the parameters of the  $\text{H}_2$  surface density law deduced from the continuum emission.

	This work ( $^{13}\text{CO}$ & continuum data)	Burrows et al. (1996) HST	Cotera et al. (2001) HST	Wood et al. (2002) HST+SED
Assumed Distance	D (pc) = 140	140	140	140
Systemic velocity	$V_{\text{lsr}}$ (km.s $^{-1}$ ) = 7.25 $\pm$ 0.04	—	—	—
Orientation (disk axis)	PA ( $^\circ$ ) = 32 $\pm$ 2	32	32	32
Inclination (disk plane)	$i$ ( $^\circ$ ) = {81 $\pm$ 3 (Best fit) 84 $\pm$ 3 (Canonical fit)}	82.5	84 (assumed)	84 (assumed)
Outer radius	$R_{\text{out}}$ (AU) = 420 $\pm$ 25	{250 (Canonical fit) 425 (Best fit)}	200 (assumed)	200 (assumed)
Turbulent linewidth	$\Delta v$ (km.s $^{-1}$ ) = 0.23 $\pm$ 0.03	—	—	—
Velocity law: $V(r) = V_{100} \left( \frac{r}{100 \text{ AU}} \right)^{-\nu}$				
Velocity at 100 AU	$V_{100}$ (km.s $^{-1}$ ) = 2.00 $\pm$ 0.09	—	—	—
Velocity exponent	$\nu$ = 0.50 $\pm$ 0.06	—	—	—
Stellar mass	$M_*$ ( $M_\odot$ ) = 0.45 $\pm$ 0.04	0.67 (assumed)	0.5 (assumed)	0.5 (assumed)
Scale Height law: $H(r) = H_{100} \left( \frac{r}{100 \text{ AU}} \right)^{-h}$				
Scale Height at 100 AU	$H_{100}$ (AU) = 22	22 (= 15.5 $\sqrt{2}$ )	21 (= 15 $\sqrt{2}$ )	24 (= 17 $\sqrt{2}$ )
Scale Height exponent	$h$ = 1.25 (assumed)	1.45	1.29 (= 58/45)	1.25 (assumed)
Temperature law: $T(r) = T_{100} \left( \frac{r}{100 \text{ AU}} \right)^{-q}$				
Temperature at 100 AU	$T_{100}$ (K) = 12 $\pm$ 1	34 (Disk surface)	—	—
Temperature exponent	$q \approx$ 0.55 $\pm$ 0.07	0.1 (= 3 - 2h)	0.4 (= 3 - 2h)	0.5 (= 3 - 2h)
H $_2$ Surface Density law: $\Sigma(r) = \Sigma_{100} \left( \frac{r}{100 \text{ AU}} \right)^{-p}$				
Surf. dens. at 100 AU	$\Sigma_{100}$ (cm $^{-2}$ ) = 3.6 $\pm$ 0.6 $10^{22}$ $\Sigma_{100}$ (g.cm $^{-2}$ ) = 0.16 $\pm$ 0.03	5.5 $10^{21}$ 0.024	— —	— —
Surf. dens. exponent	$p \approx$ 1.0	0.75 (= $s - h$ )	1.08 (= $s - h$ )	1 (= $s - h$ )
Density exponent	$s \approx$ 2.2	2.2	2.37 (assumed)	2.25 (assumed)

**Table 4.** HH 30 mm dust properties. The second column displays the best fit results while the third column shows the canonical fit results (*e.g.* obtained with a fixed outer radius of 420 AU, see text for details). The total mass is calculated assuming a gas-to-dust ratio of 100 and using the kinetic temperature derived from the  $^{13}\text{CO}$  analysis ( $T_{100} = 12$  K,  $q = 0.55$ ).

Dust: $\kappa_\nu = \kappa_o \times \left( \frac{\nu}{10^{12} \text{ Hz}} \right)^\beta$			
Absorption law	$\kappa_o$ (cm $^2$ .g $^{-1}$ ) =	0.1 (assumed)	
Dust exponent	$\beta$ =	0.4 $\pm$ 0.1	0.5 $\pm$ 0.1
Absorption at 230 GHz	$\kappa(230)$ (cm $^2$ .g $^{-1}$ ) =	0.055	0.048
Dust disk size	$R_d$ (AU) =	145 $\pm$ 20	420 (assumed)
Surface Density (H $_2$ )	$\Sigma_{100}$ (cm $^{-2}$ ) =	8.6 $10^{22}$ $\pm$ 1.4 $10^{22}$	3.6 $10^{22}$ $\pm$ 0.6 $10^{22}$
Exponent	$p$ =	0 $\pm$ 0.5	1.0 $\pm$ 0.1
Total mass	$M_{\text{disk}}$ ( $M_\odot$ ) $\approx$	2.7 $10^{-3}$ $\pm$ 0.4 $10^{-3}$	4.8 $10^{-3}$ $\pm$ 0.8 $10^{-3}$

We assumed identical gas and dust temperature at 100 AU. The best fit is obtained for a uniform disk ( $p = 0$ ) of small radius ( $150 \pm 20$  AU) and total mass  $2.7 \cdot 10^{-3} M_{\odot}$ , but solutions with a decreasing surface density and larger radii remain acceptable. Assuming the same outer radius than for CO leads to  $p = 1.1$ , and a surface density at 100 AU of  $3.6 \pm 0.3 \cdot 10^{22} \text{ cm}^{-2}$ , which corresponds to a mass of  $4.8 \cdot 10^{-3} M_{\odot}$ . Note that the mass scales inversely with the assumed dust temperature. In all cases, we find  $\beta = 0.4 \pm 0.1$ .

## 5. Outflow Model

### 5.1. Model description

While a geometrically thin disk with power law distributions of the radial dependence of density and temperature constitute a good description of circumstellar disks, no such paradigm exist for outflows. Outflow models still rely on *ad hoc* parametrization, with basic ingredients often differing from source to source.

The  $^{12}\text{CO}$  outflow of HH 30 presents a remarkably simple structure, both in terms of morphology and velocity distribution that we modelled as sketched in Fig. 9.

**Geometry** – We assume a perfect conical geometry, with an semi-opening angle  $\theta_{\text{max}}$ . The cone axis is inclined by an angle  $i$  to the line-of-sight.

**Velocity distribution** – The velocity of the outflowing gas is assumed to have two components at any position: a radial component, *i.e.* this component vector is pointing outward of the central source position and an azimuthal component (to trace a possible outflow rotation), *i.e.* a vector component tangent to the circle defined by the intersection of the outflow cone with a plane perpendicular to the jet axis.

**Density distribution and Excitation** – Our model is assuming optically thin isothermal emission: The emissivity of the gas is proportional to the local density and the brightness distribution is proportional to the column densities. The model is computed in arbitrary units, and the peak of the resulting image is further scaled to the peak of the observed maps. Our approach is thus to focus on the kinematics and morphology of the outflow rather than on the excitation conditions. We assumed that the density is located mainly along the cone edges with a constant Gaussian width scale  $w_0$  and a Gaussian decrease of the density with the distance to the star along the jet axis ( $H_0$  being the height scale).

The model is computed on a sufficiently fine grid, and is further convolved with the clean beam of the observations, in order to mimic the same angular resolution.

### 5.2. Best model

Fig. 10 shows a comparison of the  $^{12}\text{CO}$  data and of our “best” model. This comparison is composed of images of the integrated emission and of two position–velocity diagrams (perpendicular to and along the jet axis) and of the spectra integrated over the outflow. Complete sets of channel maps and position–velocity diagrams are presented in Fig. 11, 12 and 13 (electronic version only). While the  $^{12}\text{CO}$  emission clearly reveals the outflow structure, it also includes a contribution from the rotating disk and the parent cloud. Hence, we blanked out the velocities between  $4.6$  and  $9.8 \text{ km s}^{-1}$  in the data cube in order to make meaningful comparisons between data and model. While this is clear on the position–velocity diagrams and the integrated spectrum of Fig. 10, note that the integrated emission map shown as the top, left panel also excludes this velocity range. Fig. 14 and 15 (electronic version only) are variations of Fig. 10 which illustrate

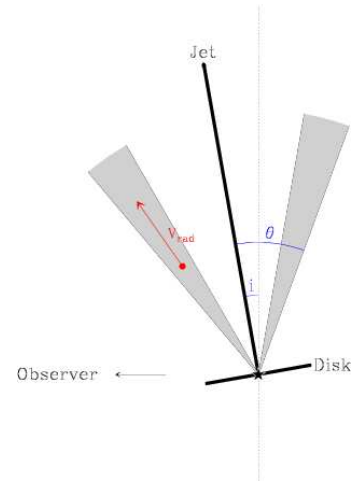


**Fig. 9.** Sketch of our outflow model. The emitting gas is confined in a layer near the edge of a conical structure (grey zone). The dotted vertical line indicates the plane of the sky. The southern part of the disk is pointed toward us in agreement with the scattered light observations (*e.g.* Burrows et al. 1996).

how the different parameters of the outflow model influence the observables.

We did not develop any  $\chi^2$  fitting procedure. We took instead the following steps to successively find a plausible range of parameters representing the data. The systemic velocity was assumed to be the same for the outflow as for the disk. The position angle was tuned to give the best averaged horizontal symmetry of the outflow on each side of the jet on the channel maps of Fig. 11. The opening angle of the cone was measured on the  $v_y$  position–velocity diagrams (Fig. 13) as the averaged slope of the minimum  $y$  value where emission is detected as a function of the  $x$  plane. The magnitude of the turbulent line width was deduced from the slope of the outer wings of the integrated spectrum. Indeed, Fig. 15 shows that the absence of turbulent line width makes infinitely sharp outer wings. Once the systemic velocity is fixed, only the inclination on the plane–of–sky ensure the correct velocity centering of the emission features in the  $v_y$  and  $xv$  position–velocity diagrams. Once the cone opening angle and the turbulent width are fixed, only the radial velocity can ensure the correct velocity width in the  $v_y$  and  $xv$  position–velocity diagrams. The density width and height scales were finally tuned to reproduce the width and height of the horn in the  $v_y$  position–velocity diagram. Table 5 lists the parameters of the “best” model and associated possible ranges of parameters. We checked that the vertical limitation of the outflow is mainly physical, *i.e.* not produced by the short-spacing filtering of the interferometer. Finally, rotation was searched for but not found (see next section).

The model depicted in Figs. 10 to 13 and Table 5 nicely reproduces the main characteristics of the HH 30 outflow, both in terms of velocity and morphology. Hence, we conclude that, to first order, the outflowing gas in HH 30 forms **a cone with a constant radial velocity distribution and no detectable rotation** (see next section). The inclination on the plane–of–sky (constrained to be essentially  $-1^\circ \pm 1^\circ$ ) indicates that this cone is nearly, but not exactly, perpendicular to the disk.

Nevertheless, a number of features are not reproduced by the model. First, our fully axisymmetric model can not reproduce the various asymmetries seen: 1) Fig. 13 illustrates that the cone opening angle is correct for negative  $\delta x$  offsets but too

**Table 5.** Outflow properties. The values in this table are model dependent. Furthermore they do not results from a fit. They thus are very different in nature from the values in the tables describing the disk which results from a validated fitting method.

	“Best”	Possible range
Assumed Distance	D (pc) = 140	(assumed)
Systemic velocity	$V_{\text{lsr}}$ (km.s <sup>-1</sup> ) = 7.25	±0.04
Orientation	PA (°) = 32	±2
Inclination	$i$ (°) = -1	±1
Half-opening angle	$\theta_{\text{max}}$ (°) = 30	±2
Turbulent linewidth	$\Delta v$ (km s <sup>-1</sup> ) = 0.40	±0.15
Velocity law: $V_r = V_{\text{rad}}, V_\theta = 0, V_\phi = V_{\text{rot}200} r^v$		
Radial velocity	$V_{\text{rad}}$ (km s <sup>-1</sup> ) = 11.5	±0.5
Rotation velocity at 200 AU	$V_{\text{rot}200}$ (km s <sup>-1</sup> ) = 0	< 1
Volume density law: $n \propto \exp\left\{-\left(\frac{r-z*\tan(\theta_{\text{max}})}{w_0}\right)^2\right\} \exp\left\{-\left(\frac{z}{H_0}\right)^2\right\}$		
Width	$w_0$ (") = 0.3	≤ 0.3
Scale Height	$H_0$ (") = 3	±0.5

small for positive  $\delta x$  offsets; 2) The position–velocity diagrams and the integrated spectra of the data clearly shows a brightness asymmetry between the [0.6, 4.2] and the [9.8, 13.4] km s<sup>-1</sup> velocity ranges. Second, the brightness distribution is more centrally peaked in the data than in the model (maybe due to heterogeneous excitation conditions). Third, there is the high velocity “clump” 1000 AU from the star along the flow axis. The associated emission shows a continuity both in the red and blue–shifted velocities with the cone emission that surrounds the optical jet (See the  $v - \delta y$  diagram in Fig. 7). This emission peak thus looks like a “clump” in the cone of outflowing gas, in contrast with standard CO “bullets” which show a distinct emission peak at velocities significantly higher than the bulk of the outflow (See e.g. Bachiller et al. 1990).

Furthermore, because of the low inclination, our observations may be insensitive to the component of motion parallel to the flow axis, because such a gas would appear at the systemic velocity and be indistinguishable from the surrounding cloud. Since we do not know the cloud extent, we can neither prove nor disprove that such a confusion is happening.

### 5.3. Rotation?

There is no strong prescription on the dependence of the rotation velocity with distance from the star and the jet axis. To test the possibility of rotation, we have introduced several rotation laws in the model: 1) constant velocity, 2) solid rotation  $V_{\text{rot}} \propto r$ , 3) Keplerian rotation, and 4) vortex rotation  $V_{\text{rot}} \propto 1/r$  (corresponding to angular momentum conservation in an expanding thin ring that would generate the outflow cone). In all those cases, rotation would manifest as a tilt of the ellipse of the  $(V, \delta x)$  position–velocity diagram (second row of Fig. 10, see also Fig. 15, left column). We selected as upper limit to  $V_{\text{rot}}$  the value that tilted the ellipse by 5°. In all cases, we can firmly rule out values of  $V_{\text{rot}}$  larger than 1 km s<sup>-1</sup> at 200 AU from the jet axis. In addition, Keplerian and vortex rotation would give rise to low level but detectable wings outside the displayed velocity range.

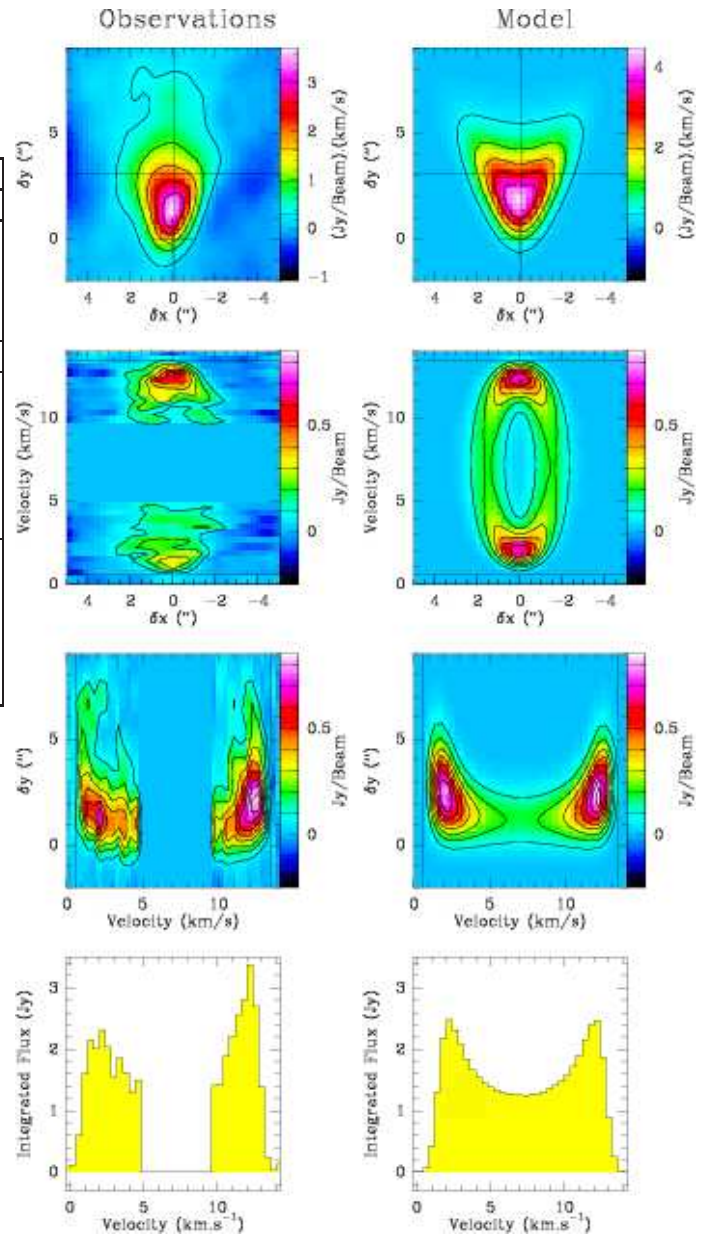


**Fig. 10.** Comparison between <sup>12</sup>CO J=2–1 observations (left column) and our best model (right column) of the outflow. The velocity channels where confusion from the disk or the parent cloud exist have been flagged in the <sup>12</sup>CO J=2–1 data cube. The integrated emission map, the position–velocity diagrams perpendicular and parallel to the jet axis and the spectrum integrated over the map are shown from top to bottom. The plots are shown in the rotated ( $\delta x, \delta y$ ) coordinate system. The horizontal and vertical lines on the integrated emission map show the position of the cuts used to form the position–velocity diagrams (respectively  $\delta x = -0.1''$  and  $\delta y = 3.1''$ ). The two horizontal or vertical lines in the position–velocity diagrams indicate the velocity range over which the emission has been integrated to form the top map ( $0.6 < V < 13.4$  km s<sup>-1</sup>).

Such wings are not detected in the complete data set, probably ruling out these kinds of rotation.

## 6. Discussion of stellar and disk parameters

### 6.1. Stellar mass estimate, luminosity and spectral type

Using a distance of 140 pc and the magnitude of the Keplerian rotation, we deduce a mass of  $0.45 M_{\odot}$  for the young star. To use this stellar mass value in a distance independent evolutionary track diagram  $\{\log(L_*/M_*^2), \log(T_{\text{eff}})\}$ , we also need the stellar luminosity value. The current estimates for HH 30 are uncertain because most of the stellar light is intercepted by the edge-on disk. Burrows et al. (1996) derived this stellar luminosity from scattered light emission at the disk surface, under the assumption of thermal equilibrium, and found (using our definition of  $H(r)$ ):

$$L = 1.0 L_{\odot} (H_{100}/22 \text{ AU})^{12} (M/0.67 M_{\odot})^6.$$

Using  $H_{100} = 22$  and  $M = 0.45 M_{\odot}$ , the corresponding luminosity is  $L = 0.1 L_{\odot}$ , with at least a factor 2 uncertainty due to the assumed scale height. Based on the analysis of the spectro-energy distribution (SED), Kenyon et al. (1994) have estimated the stellar luminosity to be  $\sim 0.2 L_{\odot}$ . More recently, Cotera et al. (2001) have estimated the luminosity to be between  $0.2$  and  $0.9 L_{\odot}$ .

Assuming  $L_* = 0.2 L_{\odot}$  as the more probable value and using Baraffe et al. (1998) tracks (see Fig. 3 of Simon et al. 2000), we find that the spectral type seems to be M3 with an age around 4-5 Million years. Note however that the tracks are almost parallel to the ordinate, *i.e.*  $\log(L_*/M_*^2)$ , in this range of mass and luminosity. A relatively small error on the luminosity leads to an important uncertainty on the age. If we take the other end of the luminosity range (*i.e.*  $0.9 L_{\odot}$ ), we get the same spectral type for an object which is less than 1 Million year old. Using the Siess et al. (2000) tracks, the spectral type would be M1-M2 with an age between 4 and 1 Myrs for a luminosity equal to  $0.2$  and  $0.9 L_{\odot}$ , respectively (see again Fig. 3 of Simon et al. 2000).

Appenzeller et al. (2005) derive a spectral type of K7 for HH 30, but caution that this results is based on a limited wavelength coverage. From Fig. 3 of Simon et al. (2000), such a spectral type is incompatible with a mass of  $0.45 M_{\odot}$  for the evolutionary tracks of Baraffe et al. (1998), Palla & Stahler (1999), and Siess et al. (2000) which fit all other sources. A K7 spectral type is compatible for the D'Antona & Mazzitelli (1997) tracks, but these fail to give agreement for the other stars. The Appenzeller et al. (2005) result nevertheless suggest that a spectral type of M3 is unlikely.

Adding the existence of a relatively powerful jet, it then seems reasonable to classify HH 30 as a young T Tauri of stellar mass  $0.45 M_{\odot}$ , spectral type ranging around M1 and age around 4 Myrs.

### 6.2. Disk Geometry

Both the mm and the optical observations reveal a disk close to edge-on. Table 3 quantitatively compares the results from both wavelength ranges. Optical & NIR observations indicate that the disk is tilted along the line of sight with  $i$  ranging from  $82$  to  $84^\circ$  (Burrows et al. 1996, and references therein). In all cases, the PA is found to be  $32^\circ$  counted anti-clockwise from North. Our results agree well with these values.

The determination of the outer radius is more model dependent. Cotera et al. (2001) and Wood et al. (2002) have assumed  $R_{\text{out}} = 200$  AU while Watson & Stapelfeldt (2004) have taken  $R_{\text{out}} = 250$  AU. All these are consistent with the minimum radius derived from the 1.3 mm continuum emission. However, in their best simulations (*i.e.* *not* the canonical one), Burrows et al.

(1996) have found  $R_{\text{out}} \simeq 440$  AU, in excellent agreement with the value derived here from  $^{13}\text{CO}$  J=2-1.

### 6.3. Disk Mass and Dust Properties

Disk masses were previously derived by several authors from NIR and optical scattered light images (Burrows et al. 1996; Cotera et al. 2001), sometimes combined with modelling of the SED (Wood et al. 2002, and references therein).

Our derived disk mass depends on three assumptions: the temperature law, the surface density exponent  $p$  and the dust emissivity. In the optical and NIR, only the upper layers of the disk surface are seen. Therefore, a detail modelling of the surface density distribution cannot be achieved without some *a priori* assumptions even though the width of the dark lane can be used to estimate the opacity law. Burrows et al. (1996) extrapolated a total disk mass of  $6 \cdot 10^{-3} M_{\odot}$ , including a correction factor of  $\simeq 15$  to account for the likely existence of a vertical temperature gradient.

Wood et al. (2002) derive a mass of  $1.5 \cdot 10^{-3} M_{\odot}$ . To do this, they use a SED fitting procedure and more sophisticated dust properties (*e.g.* with a grain size distribution) leading to an emissivity of  $\sim 40 \text{ cm}^2 \text{ g}^{-1}$  at  $0.6 \mu\text{m}$ . Wood et al. (2002) dust property implies  $\beta = 0.75$  and an emissivity of  $0.08 \text{ cm}^2 \text{ g}^{-1}$  at 1.3 mm. The difference with our determination is thus mainly due to the assumed dust properties (although the temperature and disk size also have an influence).

The value  $\beta = 0.4 - 0.5$  is at the low end of the range encountered in proto-planetary disks, and very suggestive of grain growth (*e.g.* Testi et al. 2003; Natta et al. 2004). As we have resolved the disk in its radial direction, and since our model includes the vertical distribution of the dust, this value of  $\beta$  is not biased by the contribution of an optically thick region<sup>2</sup>. However, the determination of  $\beta$  depends on the assumption that the 3.4 mm flux is due to dust emission only. A small contamination by some free-free emission from the jet would drive  $\beta$  towards lower values. Additional low frequency measurements are needed to evaluate this problem and confirm the low  $\beta$  value. Draine (2006) demonstrated that, provided the maximum grain size exceeds about  $3\lambda$  (*i.e.* 1 cm in our case), such low  $\beta$  values can be obtained for power law grains size distribution  $n(a) \propto a^{-\gamma}$  with exponent  $\gamma \simeq 3.3$ , since the apparent  $\beta$  index is linked to the material emissivity  $\beta_{\epsilon}$  by  $\beta = (\gamma - 3)\beta_{\epsilon}$ .

### 6.4. Molecular Abundances and Disk Temperature

Matching all the surface density measurements indicate a  $^{13}\text{CO}$  abundance of  $\simeq 2 \cdot 10^{-6}$ , and an  $\text{HCO}^+$  abundance of  $\simeq 2 \cdot 10^{-10}$ , with likely variations by a factor  $\simeq 2$  between 100 and 400 AU, since the column density law exponents do not necessarily match. An additional uncertainty of a factor 2 should be added due to the uncertainty in the dust emissivity at 1.3 mm.

The temperature of 12 K derived from  $^{13}\text{CO}$  data is significantly lower than the value of 34 K derived by Burrows et al. (1996). This is expected since the optically thin  $^{13}\text{CO}$  emission mostly traces the disk plane, while the scattered light traces the disk atmosphere. A decreasing temperature towards the disk plane is expected in a disk which is optically thick to the stellar radiation, but thin to its own re-emission. A rather surprising fact is that, despite this low temperature, the  $^{13}\text{CO}$  abundance

<sup>2</sup> The disk is not resolved in height, however. If the dust was confined to a very thin layer (scale height smaller than a few AU), and seen edge-on ( $i > 87^\circ$ ), an additional correction would be necessary.

suggests a low depletion of CO compared to the surrounding Taurus molecular cloud (Cernicharo & Guelin 1987), in contrast with what is found in most disks (*e.g.* Dartois et al. 2003, for DM Tau).

## 7. Discussion of outflow parameters

### 7.1. Outflow mass and energetics

In the northern lobe of the outflow, the total  $^{12}\text{CO}$  J=2–1 line flux is  $15.1 \text{ Jy km s}^{-1}$  (using only velocities in the [0.6, 4.2] and [9.8, 13.4]  $\text{km s}^{-1}$  range and integrating spatially in the area defined in Fig. 6). The  $^{13}\text{CO}$  J=2–1 line flux from the same region and velocity range is  $\approx 0.2 \pm 0.05 \text{ Jy km s}^{-1}$ . This implies a  $^{12}\text{CO}/^{13}\text{CO}$  ratio of  $\sim 80$ . Thus the  $^{12}\text{CO}$  emission is essentially optically thin. Further assuming it is at LTE allows us to derive the outflowing mass. A minimum flow mass of  $2 \cdot 10^{-5} M_{\odot}$  is found for temperatures in the range from 15 to 25 K, using a CO abundance of  $10^{-4}$ . The outflow mass scales approximately as the temperature for larger temperatures. The volume density in the outflow can be derived from its total mass and an estimate of the volume it fills. Using the conical geometry described in the previous sections and a cone thickness of 45 AU ( $0.3''$ ) we obtain a mean density  $n(\text{H}_2) \approx 8 \cdot 10^4 \text{ cm}^{-3}$ , high enough to validate the LTE assumption.

The HH 30 CO outflow presents an obvious, extremely strong asymmetry, since almost no signal is detected in its southern lobe. We estimate here the  $^{12}\text{CO}$  J=2–1 line flux to be less than about  $1.5 \text{ Jy km s}^{-1}$  (over the same velocity range as that used in the northern lobe and in a symmetric region). This implies that this side of the flow is more than 10 times less massive than the northern one. Note that, while the southern optical jet brightness is also weaker than its northern counterpart, the density ratio has been estimated to be only  $\sim 2$  (Bacciotti et al. 1999).

The physical parameters of the northern jet and outflow estimated in a region of  $\sim 6''$  or  $\sim 800 \text{ AU}$  from the central source (corresponding to the size of the maps presented in this paper) are listed in Table 6. The values for the outflow were derived from the observations presented in this paper. Those for the jet have been estimated from the literature. The mean jet density was estimated to be around  $10^4 \text{ cm}^{-3}$  by Bacciotti et al. (1999). Using a jet radius of  $0.09''$  (Bacciotti et al. 1999) and a cylindrical geometry<sup>3</sup>, the jet mass up to 800 AU is about  $2 \cdot 10^{-8} M_{\odot}$ . Burrows et al. (1996) indicates that the jet knot velocity range between  $\sim 100$  and  $300 \text{ km s}^{-1}$ , so we used a typical jet velocity of  $200 \text{ km s}^{-1}$ .

### 7.2. Formation of the outflow – entrainment?

The origin of the molecular outflows is a pending problem in star formation theories. On large scales ( $\gg 1000 \text{ AU}$ ), there is strong evidence that the observed outflows consist in ambient molecular gas that has been put into motion by large bow shocks propagating down the underlying protostellar jets (*e.g.* Gueth & Guilloteau 1999). In this classical “prompt” entrainment scenario, the jet transfers momentum to the outflow via the bow-shock, and it is usually assumed that the momentum flux is conserved in this process (*e.g.* Masson & Chernin 1992). Interestingly, this is what is indicated by our first order estimation (see table 6).

<sup>3</sup> The opening angle is only  $2^{\circ}$  beyond 100 AU, so the cylindrical approximation is appropriate

**Table 6.** HH 30 jet and outflow parameters in the northern lobe, measured in a region of  $\sim 6''$  or  $\sim 800 \text{ AU}$  from the central source (see text).

Quantity	Jet	Outflow
Mass ( $M_{\odot}$ )	$2 \cdot 10^{-8}$	$2 \cdot 10^{-5}$
Velocity ( $\text{km s}^{-1}$ )	200	12
Dynamical timescale (yr)	20	320
Mass flux ( $M_{\odot} \text{ yr}^{-1}$ )	$1.0 \cdot 10^{-9}$	$6.3 \cdot 10^{-8}$
Momentum ( $M_{\odot} \text{ km s}^{-1}$ )	$4.0 \cdot 10^{-6}$	$2.4 \cdot 10^{-4}$
Momentum flux ( $M_{\odot} \text{ km s}^{-1} / \text{yr}$ )	$2.6 \cdot 10^{-7}$	$7.5 \cdot 10^{-7}$

Viscous entrainment along the jet edges naturally results in conical shape for the outflow (Stahler 1994). However, the predicted velocities are essentially parallel to the flow axis, while our observations are essentially sensitive to the radial motions because the flow axis lies in the plane of the sky. The comparison is thus impossible in practice. The insensitivity of our observations to the gas flowing near the direction of the jet axis also implies that the outflow momentum flux we derive above is only a lower limit.

If the HH 30 outflow does indeed consist in accelerated ambient gas, the lack of CO emission in the southern lobe would point towards different properties of the interstellar medium in this direction, that would strongly alter the outflow formation process. In this context, it may be worth mentioning two similarities between HH 30 and L 1157 (Gueth et al. 1996). While the sampled scales are different (several  $10^4 \text{ AU}$  for L 1157, only a few hundreds AU in the HH 30), both outflows exhibit 1) a more or less pronounced asymmetry between their lobes and 2) a conical geometry and a radial velocity near the launching region.

### 7.3. Formation of the outflow – disk wind?

One of the most striking results revealed by our data is the fact that the outflowing molecular gas is continuously collimated down to the very close vicinity of the star, at spatial scales that are *smaller than the disk size* (see Fig. 1). This is somewhat difficult to reconcile with the propagation of a large bow-shock (see previous section). But this is naturally explained if the observed CO emission arises from material that has been directly launched from the disk and evolves ballistically in the first few 100 AU from the star. This hypothesis is also consistent with a conical flow structure, with constant radial velocity that is observed. Recollimation may occur at larger distances ( $> 1000 \text{ AU}$ ), *i.e.* outside the field-of-view of our observations.

If the outflow originates from a disk wind, we can obtain a constraint on the launch radius from the upper limit on the rotation velocity of the outflowing gas. Indeed, Anderson et al. (2003) derived a general relation between the poloidal and toroidal velocity components of cold magnetocentrifugal wind at large distance of the star and the rotation rate of the launching surface, independent of the uncertain launching conditions. This relation relies on the following facts: 1) The energy and angular momentum in the wind are extracted mostly by magnetic fields from the rotating disk; 2) The energy extracted is the work done by the rotating disk against the magnetic torque responsible for the angular momentum extraction; And 3) most of the wind energy and angular momentum at observable distances are in the measurable kinetic form. In the simple geometry of HH 30, we identify the poloidal and toroidal velocities respectively with the

radial velocity  $V_{\text{rad}}$  and the rotation velocity  $V_{\text{rot}}$  at a given radius  $r$ . The rotation rate of the launching surface is the Keplerian frequency  $\Omega_0 = \sqrt{GM_*/r_{\text{launch}}^3}$ . Anderson et al. (2003) relation:  $V_{\text{rot}} = V_{\text{rad}}^2/(2\Omega_0 r)$ , can then be transformed into

$$r_{\text{launch}} = r \left\{ 2 \frac{V_{\text{kep}}(r) V_{\text{rot}}}{V_{\text{rad}}^2} \right\}^{2/3}$$

where  $V_{\text{kep}}(r) = \sqrt{GM_*/r}$  is the Keplerian velocity at radius  $r$ . Our upper limit of  $V_{\text{rot}} < 1 \text{ km s}^{-1}$  at  $r \sim 200 \text{ AU}$  from the flow axis indicates  $r_{\text{launch}} \leq 14 \text{ AU}$ .

In this scenario, the optical jet and the outflow would be associated with different parts of the disk wind. The jet corresponds to the inner ( $< 1 \text{ AU}$ ), densest parts of the wind, which has a smaller opening angle ( $5^\circ$  half-opening angle, Bacciotti et al. 1999), larger velocities (around  $300 \text{ km s}^{-1}$ ), and recollimates closer to the disk ( $100 \text{ AU}$ ). The CO outflow would correspond to the outer part of the wind, ejected at larger radii from the star ( $5\text{--}15 \text{ AU}$ ), and could recollimate at larger distances ( $\gg 1000 \text{ AU}$ ). In terms of energetics, these observations would suggest that similar momentum fluxes are extracted from the disk at these different radii (see Table 6).

Several hypothesis could be proposed to explain the apparent discontinuity between the jet and the outflow, *i.e.* the lack of detected material at intermediate velocities and angles. We first note that the outflow cone is not totally empty; in fact, in the outflow modelling presented above, adding some material in the inner part of the jet allows us to obtain an even better fit to the data, to the price however of several new free parameters. One possible explanation is a projection effect: The outflow velocity field could lie more and more in the plane-of-sky (and thus indistinguishable from the surrounding cloud) when approaching the jet axis. The lack of significant detection could also come from temperature gradient, that would make the  $^{12}\text{CO J=2-1}$  line weaker at smaller opening angles (higher level transitions would however emit more strongly, until the gas becomes primarily atomic). Alternatively, this lack of observed emission at intermediate opening angle may be genuine, indicating that the mass loading mechanism into the disk wind is significantly more efficient at radii  $< 1 \text{ AU}$  (jet emission) and between  $\sim 5$  and  $15 \text{ AU}$  (CO flow emission, see radius estimate above) than in the intermediate zone  $\sim 1$  to  $5 \text{ AU}$ . One could further speculate that the region of the disk at the origin of the weak loading level is cooler, being *e.g.* shadowed by an inner puffed-up rim.

Finally, in this disk wind scenario, the strong difference between the northern and southern CO lobes must be related to intrinsic differences in the ejection mechanism due *e.g.* to physical differences between the northern and southern faces of the disk, or to a different magnetic configuration. HH 30 also presents other, second-order, asymmetries. Optical studies indicate that the jet is currently perpendicular to the disk axis (Burrows et al. 1996); our measurements however suggest a slight misalignment between the flow axis and the jet/disk axis, the inclinations differing by  $6 \pm 3^\circ$ . In the MHD wind model discussed here, this suggests the magnetic field does not have a symmetric pattern around the disk axis. An additional complexity is the fact that, at slightly larger scales ( $\sim 3000 \text{ AU}$ ), the jet is wobbling around its mean direction by  $\pm 3^\circ$  (Burrows et al. 1996). This is an indication of a precession (or more generally wandering) of the ejection direction. However, the data presented in this paper do not probe the properties of the molecular outflow at this scale.

## 8. Conclusions

In the HH 30 case, a judicious use of the complementary line emission allowed us to derive a number of very robust results: 1) The systemic velocity of HH 30 is  $7.25 \text{ km s}^{-1}$ ; 2) The disk outer radius is  $420 \text{ AU}$ ; 3) The rotation vector of the disk points toward the North-Eastern jet; 4) The disk is in Keplerian rotation; 5) The stellar mass is  $0.45 M_\odot$ ; 6) A highly asymmetric molecular outflow originates from the inner parts of the disk; 7) The outflow material is mainly located on the thin edges of a cone with an opening angle of  $30^\circ$ ; 8) The outflow velocity is essentially radial with a magnitude of  $12 \text{ km s}^{-1}$ ; 9) No rotation of the outflow is detected.

The total disk mass is less certain:  $\sim 4 \cdot 10^{-3} M_\odot$ . This depends on the assumed dust emissivity. Our measurement indicate a rather low value of  $\beta$ ,  $0.4$ , suggestive of significant grain growth. In addition, but with still less certainty, the disk appears cold, around  $12 \text{ K}$  at  $100 \text{ AU}$ , suggesting a significant temperature gradient between the disk plane and the surface layers. Despite this low temperature, there is no measurable depletion of CO compared to the average abundance in the Taurus cloud, in contrast with the general trend for all other circumstellar disks (except those around H Ae stars, see Pietu et al. 2006).

The direct determination of the stellar mass improves the evolutionary status of HH 30, but this remains hampered by the uncertainties on the total luminosity. The most plausible solution is that of a  $\sim 4 \text{ Myr}$  old object, with a total luminosity of order  $0.2 L_\odot$ , but a younger and brighter star cannot be excluded.

Finally, the origin of the molecular outflow remains unclear, with no conclusive arguments to distinguish between an entrainment mechanism by the optical jet or a disk wind. The one sided nature of the outflow remains an unexplained issue in both hypothesis.

*Acknowledgements.* We acknowledge the IRAM staff at Plateau de Bure and Grenoble for carrying out the observations. JP thanks S. Cabrit for useful comments on jet and outflow models and M. J. Welch for providing the  $^{13}\text{CO J=1-0}$  spectra cube of the HL Tau environment. We thank both the editor C. Bertout and the referee R. Bachiller for their comments that helped to improve the paper.

## References

- Anderson, J. M., Li, Z.-Y., Krasnopolsky, R., & Blandford, R. D. 2003, *ApJ Lett.*, 590, L107
- Appenzeller, I., Bertout, C., & Stahl, O. 2005, *A&A*, 434, 1005
- Arce, H. G., Shepherd, D., Gueth, F., et al. 2006, in *Protostars and Planets V*, <http://www.ifa.hawaii.edu/UHNAI/ppv.htm>
- Bacciotti, F., Eisloffel, J., & Ray, T. P. 1999, *A&A*, 350, 917
- Bacciotti, F., Ray, T. P., Eisloffel, J., et al. 2003, *Ap&SS*, 287, 3
- Bachiller, R., Martin-Pintado, J., Tafalla, M., Cernicharo, J., & Lazareff, B. 1990, *A&A*, 231, 174
- Baraffe, I., Chabrier, G., Allard, F., & Hauschildt, P. H. 1998, *A&A*, 337, 403
- Burrows, C. J., Stapelfeldt, K. R., Watson, A. M., et al. 1996, *ApJ*, 473, 437
- Cernicharo, J. & Guelin, M. 1987, *A&A*, 176, 299
- Coffey, D., Bacciotti, F., Woitas, J., Ray, T. P., & Eisloffel, J. 2004, *ApJ*, 604, 758
- Cotera, A. S., Whitney, B. A., Young, E., et al. 2001, *ApJ*, 556, 958
- D'Antona, F. & Mazzitelli, I. 1997, *Memorie della Societa Astronomica Italiana*, 68, 807
- Dartois, E., Dutrey, A., & Guilloteau, S. 2003, *A&A*, 399, 773
- Draine, B. T. 2006, *ApJ*, 636, 1114
- Dutrey, A., Guilloteau, S., & Ho, P. 2006, in *Protostars and Planets V*, <http://www.ifa.hawaii.edu/UHNAI/ppv.htm>
- Dutrey, A., Guilloteau, S., & Simon, M. 1994, *A&A*, 286, 149
- Gueth, F. & Guilloteau, S. 1999, *A&A*, 343, 571
- Gueth, F., Guilloteau, S., & Bachiller, R. 1996, *A&A*, 307, 891
- Guilloteau, S. & Dutrey, A. 1998, *A&A*, 339, 467
- Kenyon, S. J., Dobrzycka, D., & Hartmann, L. 1994, *AJ*, 108, 1872
- Koerner, D. W., Sargent, A. I., & Beckwith, S. V. W. 1993, *Icarus*, 106, 2
- Konigl, A. & Pudritz, R. E. 2000, *Protostars and Planets IV*, 759

- Mannings, V., Koerner, D. W., & Sargent, A. I. 1997, *Nat*, 388, 555
- Masson, C. R. & Chernin, L. M. 1992, *ApJ Lett.*, 387, L47
- Natta, A., Testi, L., Neri, R., Shepherd, D. S., & Wilner, D. J. 2004, *A&A*, 416, 179
- Palla, F. & Stahler, S. W. 1999, *ApJ*, 525, 772
- Pety, J. 2005, in SF2A-2005: Semaine de l'Astrophysique Francaise, ed. F. Casoli, T. Contini, J. M. Hameury, & L. Pagani, 721–+
- Pietu, V., Dutrey, A., & Guilloteau, S. 2006, in preparation
- Pringle, J. E. 1981, *ARAA*, 19, 137
- Rodder, C., Rodder, F., Northcott, M. J., Graves, J. E., & Jim, K. 1996, *ApJ*, 463, 326
- Shu, F. H., Najita, J. R., Shang, H., & Li, Z.-Y. 2000, *Protostars and Planets IV*, 789
- Siess, L., Dufour, E., & Forestini, M. 2000, *A&A*, 358, 593
- Simon, M., Dutrey, A., & Guilloteau, S. 2000, *ApJ*, 545, 1034
- Stahler, S. W. 1994, in *ASP Conf. Ser. 65: Clouds, Cores, and Low Mass Stars*, ed. D. P. Clemens & R. Barvainis, 330–+
- Stapelfeldt, K. & The WFPC2 Science Team. 1997, in *Science with the VLT Interferometer*, 395–+
- Stapelfeldt, K. R. & Padgett, D. L. 1999, in *Science with the Atacama Large Millimeter Array (ALMA)*
- Stapelfeldt, K. R., Watson, A. M., Krist, J. E., et al. 1999, *ApJ Lett.*, 516, L95
- Testi, L., Natta, A., Shepherd, D. S., & Wilner, D. J. 2003, *A&A*, 403, 323
- Watson, A. M. & Stapelfeldt, K. R. 2004, *ApJ*, 602, 860
- Welch, W. J., Hartmann, L., Helfer, T., & Briceño, C. 2000, *ApJ*, 540, 362
- Wood, K., Wolff, M. J., Bjorkman, J. E., & Whitney, B. 2002, *ApJ*, 564, 887
- Wood, K., Wolk, S. J., Stanek, K. Z., et al. 2000, *ApJ Lett.*, 542, L21

# Online Material

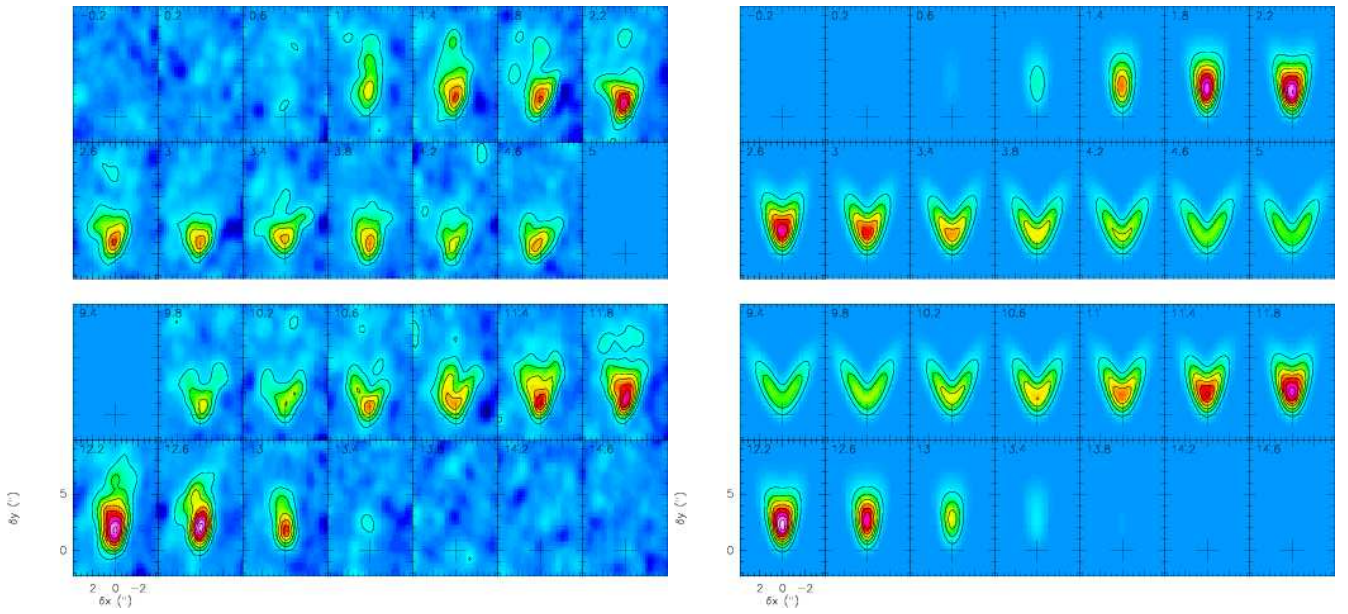


**Fig. 11.** Comparison of the *channel maps* of the  $^{12}\text{CO}$  J=2–1 observations (left) and our best model (right) of the outflow. The cross indicates the disk center as measured in the 1.3 mm continuum emission. Velocity of the channels are written in  $\text{km s}^{-1}$  on the top left corner of each channel. Both channel maps share the same color scale and contour spacing (0.1 Jy/beam).

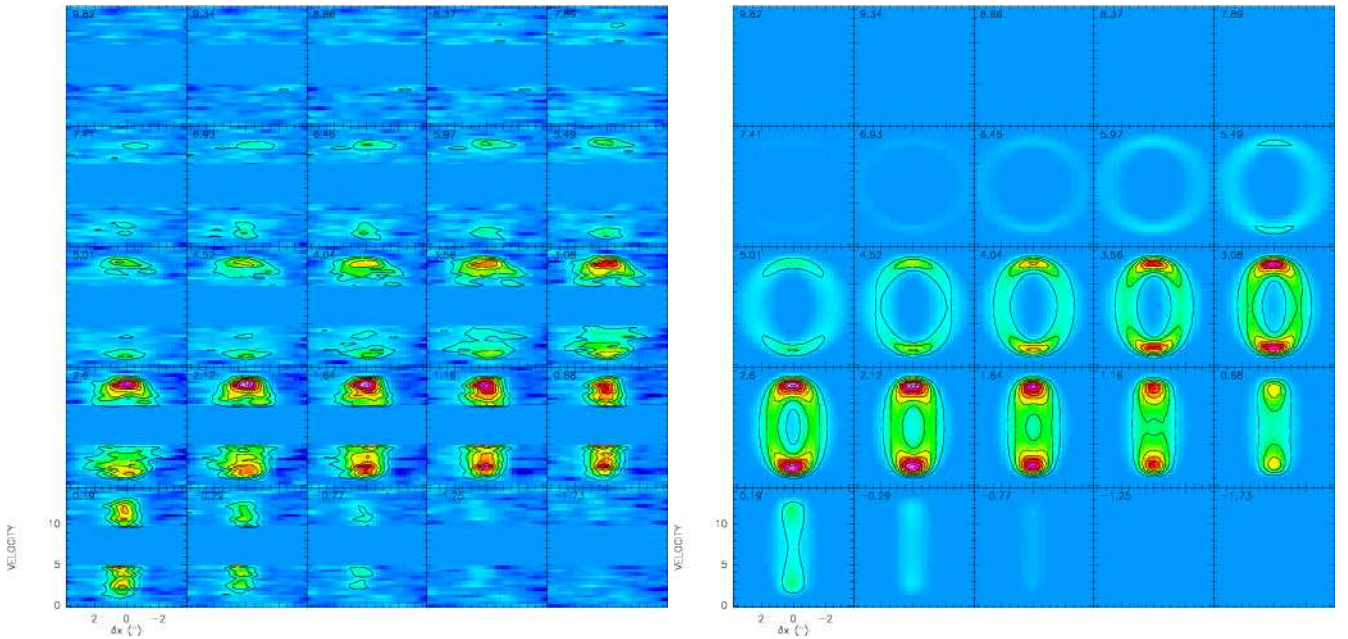


**Fig. 12.** Comparison of the *position–velocity diagrams perpendicular to the jet axis* of the  $^{12}\text{CO}$  J=2–1 observations (left) and our best model (right) of the outflow. The coordinate along the jet axis ( $\delta y$ ) are written in arcsecond on the top left corner of each panel. All the diagrams share the same color scale and contour spacing (0.1 Jy/beam).

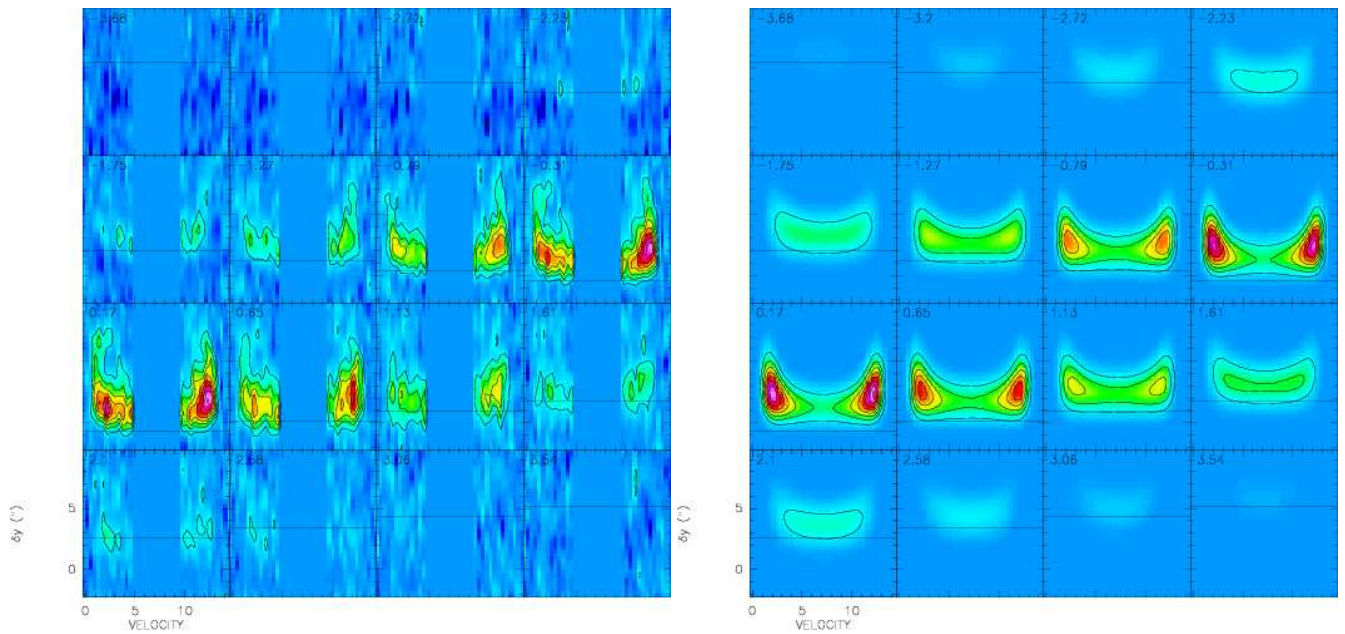


**Fig. 13.** Comparison of the *position–velocity diagrams* along the jet axis of the  $^{12}\text{CO}$  J=2–1 observations (left) and our best model (right) of the outflow. The coordinate perpendicular to the jet axis ( $\delta x$ ) are written in arcsecond on the top left corner of each panel. The horizontal line indicates the position of the outside edge of a cone of  $30^\circ$  half opening–angle. All the diagrams share the same color scale and contour spacing (0.1 Jy/beam).

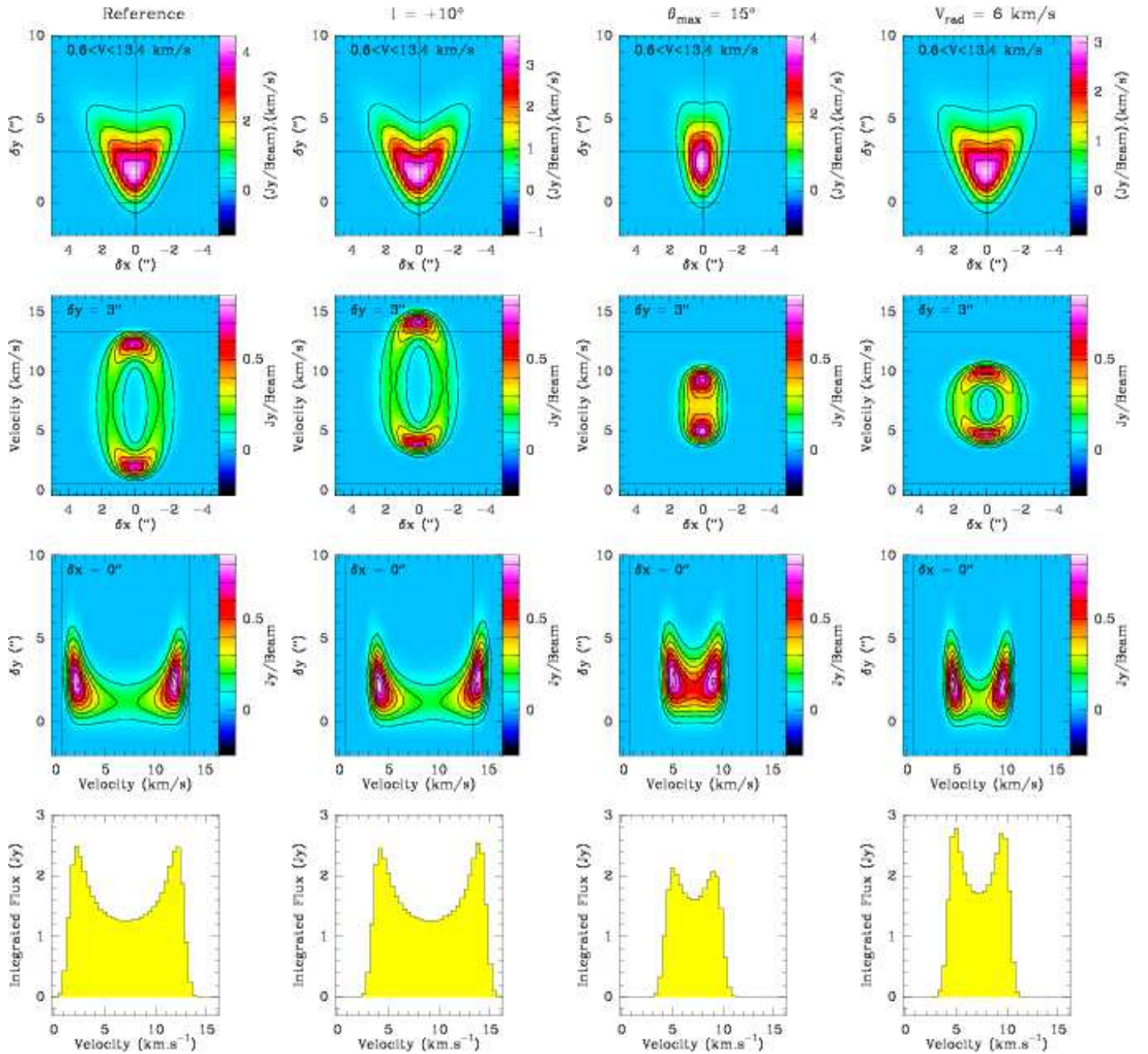


**Fig. 14.** Influence of the different parameters of the outflow model. The left column shows our reference model whose parameters are given in Table 5. The each column shows a model for which one and only one parameter (noted on the column top) has been varied compared to our reference model. The integrated emission map, the position–velocity diagrams perpendicular and parallel to the jet axis and the spectrum integrated over the map are shown from top to bottom.

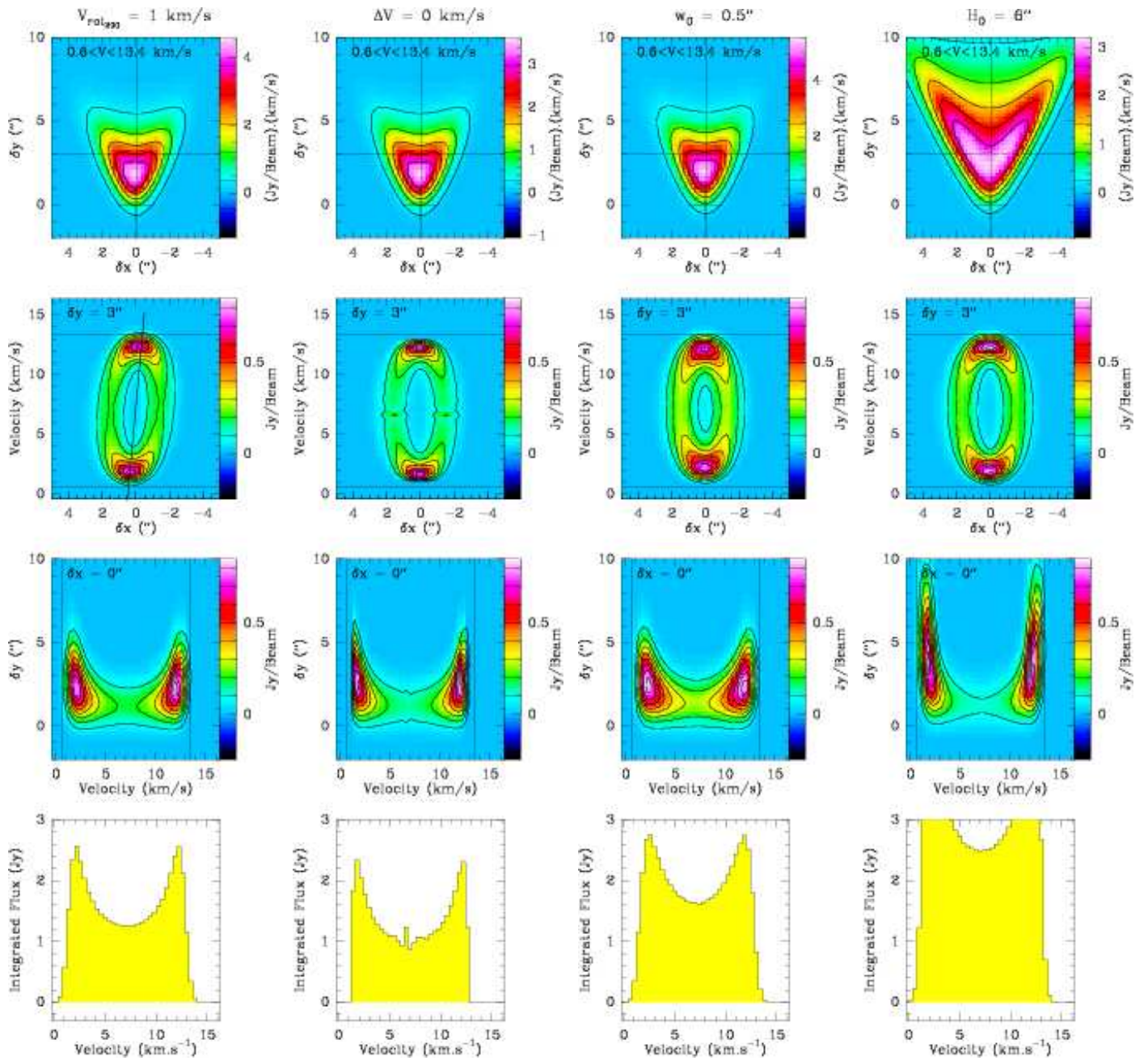


Fig. 15. Continuation of Fig. 14 with different varying parameters.